ACTA MATERIALIA TRANSYLVANICA

Material Sciences Publications

Volume 5, Issue 1

ERDÉLYI MÚZEUM-EGYESÜLET
Cluj-Napoca
2022

The publication of this magazine was supported by the Hungarian Academy of Sciences, by the Bethlen Gábor Fund and by the TMS – Department of Engineering Sciences

Publisher: Erdélyi Múzeum-Egyesület
Responsible publisher: Biró Annamária
Proofreader: Szenkovics Enikő (Hu), David Speight (En)
Editorial secretary: Kisfaludi-Bak Zsombor
Cover: Könczey Elemér
Printed at: F&F International Kft., Gyergyószentmiklós

ISSN 2601-1883, ISSN-L 2601-1883
DOI: 10.33923/amt-2020-02
The journal website: https://www.eme.ro/publication/acta-mat/mat-main.htm

Acta Materiala Transylvanica – Material Sciences Publications – is a journal of the Technical Sciences Department of the Transylvanian Museum Society, publishing scientific papers, issues, reviews and studies in the field of material sciences. Its mission is to provide and disseminate a comprehensive picture focusing on research trends and scientific results in the Carpathian basin. In accordance with the general mission of the Transylvanian Museum Society it aims to support specialized literature in Hungarian. The printed version of the journal is published in Hungarian and is available in the Transylvanian Digital Database (https://eda.eme.ro/handle/ 10598/30356). However, we would like to spread it internationally, therefore the full content of the journal will also be available in English.

Content

sciendo

Acta Materialia Transylvanica 5/1. (2022) 1–5.
DOI: Hungarian: https://doi.org/10.33923/amt-2022-01-01
English: https://doi.org/10.33924/amt-2022-01-01

ACTA MATERIALIA TRANSYLVANICA

Simulation of CuE Copper Alloy in a Closed-Die Multi-Axial Forging Tool

Tamás BÍRÓ,[1] Zsombor JUHÁSZ,[2] József Bálint RENKÓ[3]

[1] *Budapest University of Technology and Economics, Department of Materials Science and Engineering, Faculty of Mechanical Engineering, Budapest, Hungary, biro.tamas@edu.bme.hu*

[2] *Budapest University of Technology and Economics, Department of Materials Science and Engineering, Faculty of Mechanical Engineering, Budapest, Hungary, juhasz.zsombor@edu.bme.hu*

[3] *Budapest University of Technology and Economics, Department of Materials Science and Engineering, Faculty of Mechanical Engineering, Budapest, Hungary, renko.jozsef@edu.bme.hu*

Abstract

Two-way multi-axial forging was performed on a newly designed closed-die forging tool. The tool was operated on an MTS 810 material testing system. The connected computer recorded force and crosshead displacement as a function of time during operation. The sample material of the four-step forging experiment was CuE copper alloy. The plastic deformation was 0.8 per step, thus the rate of cumulative equivalent plastic strain was 3.2 by the end of the process. The speed of movement of the active tools during the whole test was 2 mm/min. Finite element simulation was performed with QForm3D software to investigate the force conditions of the process. The necessary flow curve was determined by Watts-Ford test. The force-displacement curves of the physical simulation were compared with the results of the finite element modeling.

Keywords: *multi-axial forging, finite element modeling, Watts-Ford test.*

1. Introduction

In recent years ultrafine and nanograined materials have become very popular in materials science[1]. This is due to their more favourable mechanical properties compared to the same quality coarse-grained materials. Ultrafine grain structure can result in increased strength, higher fatigue limits, and increased toughness [2–3]. There are several methods to create these materials [4–6]. Those that apply significant shear stress on the material are called severe plastic deformation (SPD) processes [7–9]. Multi-axial forging is one of these methods [10–11].

Earlier a newly designed, closed-die forging tool was developed to investigate the mechanical properties of materials that can be produced by multi-axial forging. Our aim was to investigate the force history of a four-step forming with this new tool. Additionally, the previously implemented physical simulation was recreated with finite element modeling. Thus, we could compare the recorded force-displacement curves and draw conclusions about the reliability of the finite element model.

2. Experimental

2.1. Material

In order to keep the tool loads at a controllable level, a suitably soft material had to be selected as workpiece. Thus, the chosen material was industrial grade copper. The chemical composition of the CuE material was measured by EDAX Z2 type SEM-EDS system, but it could not detect a significant amount of impurities. The workpiece nominal dimensions were $10 \times 10 \times 20$ mm. This geometry was machined from block material. To reach the softest state of the material, the workpiece was placed in an oven preheated to 950 °C, and after 15 minutes of holding at this temperature, it was put into cold water. This heat treatment eliminated the effects of aging and the unknown deformation history prior to the tests [12].

2.2. Equipment

The tool used for physical simulations is composed of three main parts as shown in Figure 1. lThe first part is the center block, where the forging takes place. The second part is the tool housing, which frames the other components and ensures the relative position of the individual parts to one another.

Finally, linear actuators are included to provide the tool movements required for forming. The four self-moving stamps are connected by the tool housing. Thus, the stamps facing each other always move together, but with a maximum displacement of no more than 5-5 mm.

An MTS 810 universal material testing system was used to implement the necessary tool movements and to record the displacement and force data as a function of time. The maximal measuring limit of the equipment was 250 kN. During forging, the movement speed of the crosshead was 4 mm/min, which results a 2 mm/min movement speed for each tool.

To minimize tool loads, the friction had to be reduced. To achieve this, proper lubrication of the workpiece and the forming cavity was essential [13]. Surfaces directly contacting the workpiece were coated with zinc stearate paste prior to testing. Due to the closed nature of the die cavity, the cover plate must be temporarily removed for lubrication and insertion of the workpiece, and then reattached before the first forming step.

At the end of the current forging step, the tool returns to its initial position. The geometry of the workpiece is the same as the initial one, but rotated 90 ° in space. Due to the symmetrical design of the tool, with a 90 ° rotation, the relative position of the tool and the workpiece to the MTS system can be reset without opening the tool forming cavity. After rotating the whole tool, the next forming step follows.

2.3. Physical simulations

During the physical simulations four consecutive forming steps were performed, while the displacement of the crosshead and the force were recorded as the function of time. Figure 2 shows the first two forging steps, as they are representative of the whole cyclic process.

Assuming a plane strain state, the logarithmic deformation of the workpiece is approximately 0.80. (1)

$$\varphi = \frac{2}{\sqrt{3}} \cdot ln\left(\frac{H}{h}\right) = \frac{2}{\sqrt{3}} \cdot ln\left(\frac{20}{10}\right) = 0.80 \quad (1)$$

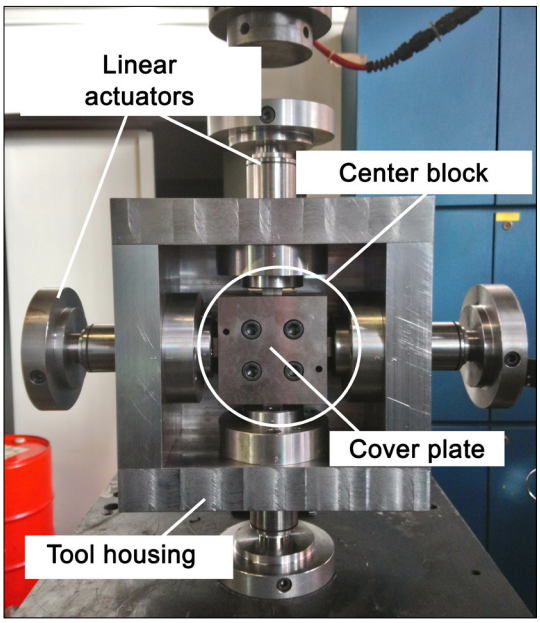

Figure 1. *General construction and main parts of the used closed-die multi-axial forging tool*

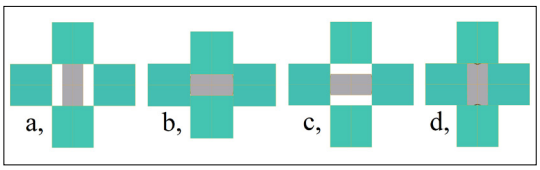

Figure 2. *Schematic figure of two consecutive forming steps while maintaining the position of the workpiece (gray). Starting position (a), final state of the first forging step (b), tools move back to their initial position (c), end of the second forging step (d)*

where φ is the plastic strain, H is the initial height of the workpiece and h is the workpiece height measured at the end of the forging step [14].

The cumulative plastic deformation (φ_{kum}) can accordingly be calculated as the sum of the plastic strains achieved in each forging step (2). In the 4-step forming process presented in the current study, its value is 3.2.

$$\varphi_{kum} = 4 \cdot \frac{2}{\sqrt{3}} \cdot ln\left(\frac{20}{10}\right) = 3.2 \quad (2)$$

2.4. Finite element modeling

A finite element model was developed to reproduce and analyse the multi-axial forging process. To create the finite element model, QForm3D software was used. 3D models can give more accurate

results of the process than 2D models, but their computation requirements are significantly higher. Due to the arrangement of the tools and the symmetry of their movements, it is sufficient to use an eighth model, which can reduce the maximum number of elements and, consequently, the required computational time. The nominal dimensions of the tool and the workpiece were used to create the necessary geometry, and the displacement-time data measured during the physical simulations were used for the tool movements [15]. The assembled model is shown in Figure 3.

The finite element mesh was automatically created by the software. Additionally, the workpiece was remeshed in each calculation step. Mesh refining was also applied in the contact area between the workpiece and the tool. For the whole process tetragonal elements were used. Their initial number was 29069, but by the end of the simulation, this had increased to 33748 due to continuous mesh refinement.

The flow curve used in the calculations was measured by Watts-Ford test on a specimen prepared under the same conditions as the workpiece [16]. It is important to point out that the maximum plastic strain here was only 2.97, so the stress-strain curve beyond this value was generated by the program based on the fitted curve (Figure 4).

3. Results and discussion

The change of force as a function of displacement measured during the physical simulations is shown in Figure 5.

Within each forming step, the force increased monotonically, and the force requirement of each forming step increased with the number of forming steps. At the end of the first three steps, the increase in force was nearly the same at 10 kN. Thereafter, the increment in force was reduced, and the force of the fourth step did not change significantly compared to the previous step. The dislocation density of the softened copper is presumably no longer increasing after the third forming step to such an extent that it causes a significant increase in the force [17].

The force-displacement curves of the finite element model show a similar trend with the results of the physical simulation (Figure 6).

As the forming steps progress, the force also increases step by step, and maintains its monotonous nature within a given step. In contrast to the

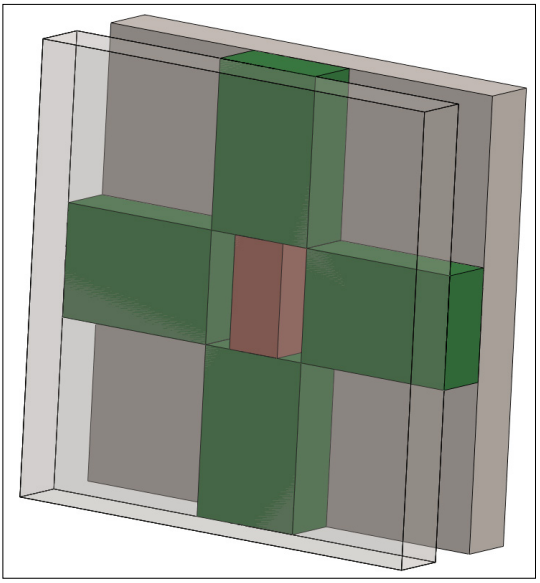

Figure 3. *The 3D models used in the simulation.*

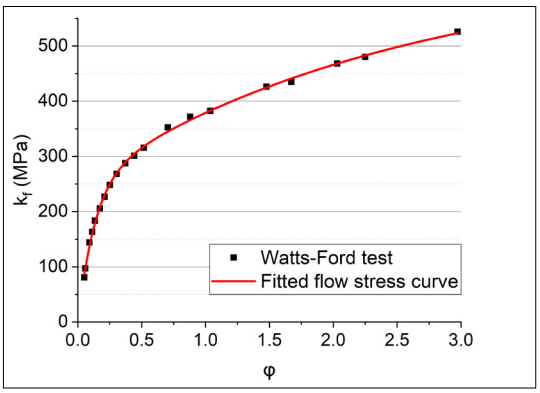

Figure 4. *Watts–Ford test result and flow curve fitted to the data.*

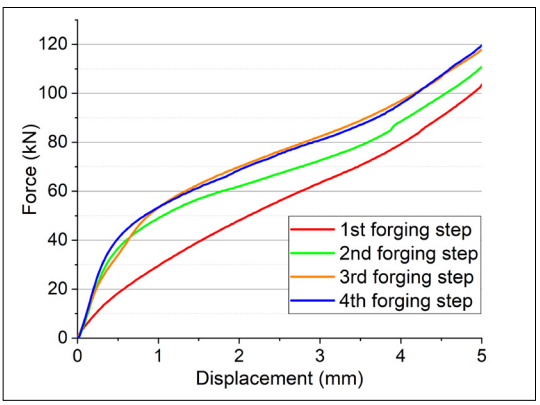

Figure 5. *Force-displacement curves obtained by the physical simulation of multi-axial forging.*

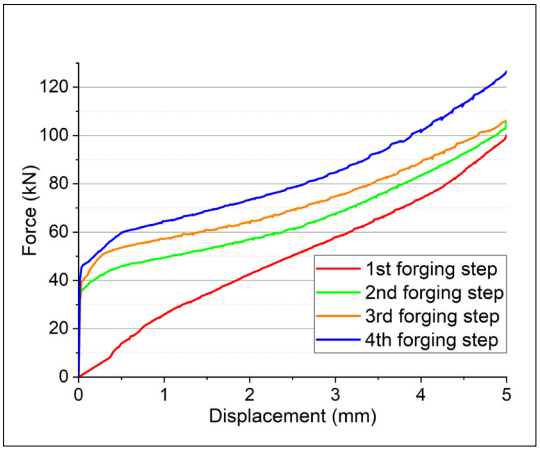

Figure 6. *Force-displacement curves obtained by finite element modeling.*

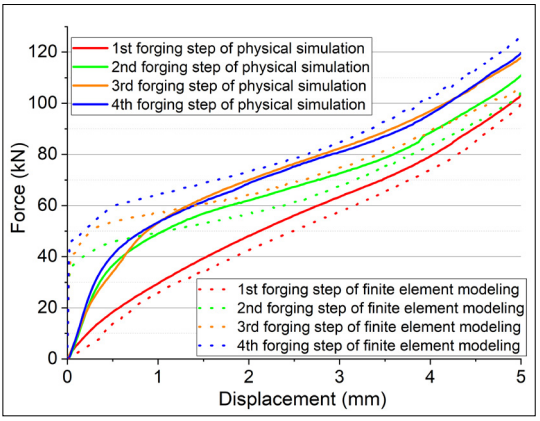

Figure 7. *Comparison of force-displacement curves resulting from physical simulation and finite element modeling.*

physical simulation, the force increase at the end of the first three steps is only about 5 kN. By the end of the fourth step, the force shows a drastic increase. The reason for this is presumably that the flow stress curve recorded by the Watts-Ford test was not measured over the entire test range, and in the second half of the fourth step, the fitted curve presumably rose steeper than reality.

By fitting the curves of the physical and finite element simulations to each other, for a given forging step the curve of the physical simulation is located slightly below the curve of the finite element model (**Figure 7**).

An exception to this trend is the curve for the fourth forging step, where the force values obtained with the finite element model jump drastically. This can be traced back to several reasons. On one hand, it can be assumed that the fitted flow-stress curve does not flatten after leaving the studied deformation range of Watts-Ford test as it would in reality. On the other hand, the difference may also be related to the deformation history of the workpiece. The tests were preceded by a softening heat treatment, so the deformation of the material could start from an almost isotropic state and could be transformed into an anisotropic structure during forging. The effect of this on the macroscopic properties presumably reached the extent that it could be detected in the third and fourth forming steps.

4. Conclusions

We performed successful experiments with a closed-die multi-axial forging tool. The four forming steps were performed by rotating the tool 90° after each step without opening the die cavity. Examining the obtained force-displacement curves, the measured force increased step by step. These characteristics were also supported by the finite element model of the process. The differences in the finite element model, especially those experienced during the fourth forming step were caused by the differences in the test ranges of the physical simulation and the Watts-Ford test. The finite element model was able to approximate reality, but to improve its accuracy it is necessary to refine the applied material model.

Acknowledgement

Supported by the ÚNKP-21-2-I-BME-218 New National Excellence Program of the Ministry for Innovation and Technology from the source of the National Research, Development and Innovation Fund.

The publication of the work reported herein has been supported by GMKA at BME.

References

[1] Huang Y., Langdon T. G.: *Advances in ultrafine-grained materials*. Materials Today 16/3. (2013) 85–93. https://doi.org/10.1016/j.mattod.2013.03.004

[2] Valiev R. Z., Islamgaliev R. K., Alexandrov I. V.: *Bulk nanostructured materials from severe plastic deformation.* Progress in Materials Science, 45. (2000) 103–189. https://doi.org/10.1016/S0079-6425(99)00007-9

[3] Langdon T. G.: *The principles of grain refinement in equal-channel angular pressing.* Materials Science and Engineerig A, 462. (2007) 3–11. https://doi.org/10.1016/j.msea.2006.02.473

[4] Segal V. M., Reznikov V. I., Drobyshevkij A. E. Kopylov V. I.: *Plastic Working of Metals by Simple Shear*. Russian Metallurgy, 1. (1981) 99–105.

[5] Toth L. S., Vu V. Q., Dhinwal S. S., Zhao Y., Massion R., Chen C., Davis C. F., Lowe T. C.: *The mechanics of High Pressure Compressive Shearing with application to ARMCO® steel.* Materials Characterization, 154. (2019) 127–137. https://doi.org/10.1016/j.matchar.2019.05.039

[6] Szabó P. J., Bereczki P., Verő B.: *The Effect of Multiaxial Forging on the Grain Refinement of Low Alloyed Steel.* Periodica Polytechnica Mechanical Engineering, 55/1. (2011) 63–66. https://doi.org/10.3311/pp.me.2011-1.09

[7] Huang Y., Langdon T. G.: *Advances in ultrafine-grained materials.* Materials Today, 16/3. (2013) 85–93. https://doi.org/10.1016/j.mattod.2013.03.004

[8] Jin X., Chena S., Rong L.: *Microstructure modification and mechanical property improvement of reduced activation ferritic/martensitic steel by severe plastic deformation.* Materials Science & Engineering A, 712. (2018) 97–107. https://doi.org/10.1016/j.msea.2017.11.095

[9] Sadasivan N., Balasubramanian M.: *Severe plastic deformation of tubular materials – Process methodology and its influence on mechanical properties – A review.* Materials Today: Proceedings, 46. (2021) 3460–3468. https://doi.org/10.1016/j.matpr.2020.11.859

[10] Trivedi P., Nune K. C., Misra R. D. K., Goel S., Jayganthan R., Srinivasan A.: *Grain refinement to submicron regime in multiaxial forged Mg-2Zn2Gd alloy and relationship to mechanical properties.* Material Science and Engineering: A, 668. (2016) 59–65. https://doi.org/10.1016/j.msea.2016.05.050

[11] Naser T. S. B., Krállics G.: *The effect of multiple forging and cold rolling on bending and tensile behavior of Al 7075 alloy.* Materials Science Forum, 729. (2012) 464–469. http://doi.org/10.4028/www.scientific.net/MSF.729.464

[12] Chen X., Zhao G., Xu X., Wang Y.: *Effects of heat treatment on the microstructure, texture and mechanical property anisotropy of extruded 2196 Al Cu Li alloy.* Journal of Alloys and Compounds, 862. (2021) 158102. https://doi.org/10.1016/j.jallcom.2020.158102

[13] Wilson W. R. D.: *Friction and Lubrication in Bulk Metal-Forming Processes.* Journal of Applied Metalworking, 1. (1978) 7–19.

[14] Valberg H. S.: *Applied Metal Forming.* Cambridge University Press, (2010) 53–76.

[15] Zienkiewicz O. C., Taylor R. L.: *The Finite Element Method. Solid Mechanics.* 5. kiadás. Butterworth-Heinemann, Oxford, 2000. 1–21.

[16] Watts A.B., Ford H.: *On the Basic Yield Stress for a Metal.* Proceedings of the Institution of Mechanical Engineers, 169/1. (1955) 1141–1156.

[17] Shakhova I., Yanushkevich Z., Fedorova I., Belyakov A., Kaibyshev R.: Grain refiment in a Cu Cr Zr alloy during multidirectional forging. Material Science and Engineering, 606. (2014) 380–389.

sciendo

Acta Materialia Transylvanica 5/1. (2022) 6–9.
DOI: Hungarian: https://doi.org/10.33923/amt-2022-01-02
English: https://doi.org/10.33924/amt-2022-01-02

ACTA MATERIALIA TRANSYLVANICA

Estimation of Dislocation Distribution at Mid Thickness for 1050 Al

Purnima CHAKRAVARTY,[1, 2] Gyula PÁL,[1, 2] János Gy. BÁTORFI,[1, 2] Jurij J. SIDOR[1]

[1] *Savaria Institute of Technology, Faculty of Informatics, Eötvös Loránd University, Szombathely, Hungary*

pc@inf.elte.hu (P.C), pg@inf.elte.hu (P. Gy.), bj@inf.elte.hu (B. J. Gy.), js@inf.elte.hu (J.S)

[2] *Doctoral School of Physics, Faculty of Natural Sciences, Eötvös Loránd University, Budapest, Hungary*

Abstract

The current study reports three different techniques to estimate the distribution of dislocation density at the mid thickness of 1050 Al alloy. It is well known that the strain distribution is inhomogeneous through the thickness of rolled materials, which affects the evolution of dislocation density during the process of deformation. In this study, the number of dislocations was calculated experimentally using indentation technique in 46.8 % cold rolled 1050 Al sheet and the result was verified by two numerical methods.

Keywords: *dislocation density, microhardness, numerical models.*

1. Introduction

Aluminum alloys consist of high strength-to-weight ratio and hence are extensively used as a structural material in aerospace, manufacturing, transportation and mobile communication industries, enabling products with lower fuel consumption and environmental impact. However, most of the aluminum is used in the form of a sheet product, which is produced through numerous rolling schedules [1]. It is well known that plastic deformation enhances the quantitative amount of linear defects in materials, thereby increasing the work hardening of the final product [1, 2]. To efficiently study the work hardening effect due to different deformation techniques such as reducing material thickness by rolling, it is important to estimate the dislocation density (ρ) of the material [2]. On the other hand, at microscopic levels, the deformation mechanism is found to be inhomogeneous, which involves heterogeneous density distribution of dislocation throughout the material [3]. The inhomogeneous strain distribution over the thickness of a material can affect the work hardening of the respective area [1–3], which makes it important to extend the distribution of dislocations over the thickness.

In the present study, to calculate the dislocation density of mid thickness of the sample, one experimental method, i.e., indentation technique, and two numerical models, i.e., Kubin-Estrin (K-E) and modified K-E have been employed. By employing the indentation technique, the dislocation density can be calculated from the hardness response of the material [4–5], using following relation:

$$\boldsymbol{\rho} = \frac{1}{\alpha^3}\left(\frac{H_V}{3.06\, M G b}\right)^2 \tag{1}$$

In equation (1), H_V is the Vickers Hardness, M is a Taylor factor, G is the shear modulus, b is the Burgers vector and α stands for the geometric constant.

There are modelling techniques enabling the calculation of dislocation density. For instance in the K-E model the total dislocation density ρ is evaluated as the sum of forest ρ_f and mobile ρ_m dislocations. Both ρ_f and ρ_m are variable functions of the applied strain (ε) [6]:

$$\frac{d\rho_m}{d\varepsilon} = C_1 - C_2\rho_m - C_3\rho_f^{\frac{1}{2}} \tag{2}$$

$$\frac{d\rho_f}{d\varepsilon} = C_2\rho_m + C_3\rho_f^{\frac{1}{2}} - C_4\rho_f \tag{3}$$

In equations (2) and (3), the coefficients C_1 and C_2 stand for the multiplication of mobile dislocations and their significant trapping, whereas the immobilization via interaction with the forest dislocations is represented by the C_3 parameter. The C_4 parameter governs the dynamic recovery.

The K-E model was further simplified by Csanádi et al. by bringing the forest and mobile terms of dislocation density together and thereby reducing the number of modeling parameters. The modified K-E model is given as [7] :

$$\rho(\varepsilon) = \frac{2C_1}{C_4} - \left(\frac{2C_1}{C_4} - \rho_0\right)\left(1 + \frac{C_4\varepsilon}{2}\right) exp(-C_4\varepsilon) \quad (4)$$

For aluminum alloys the parameter: C_1 = 2.33×10^{14} m^{-2} and C_4 = 1.15 [8].

The present research aims to study the quantitative characteristics of dislocations accumulated at the core of a 46.8 % deformed 1050 Al sheet, using the above-mentioned techniques. Geometrically, the core of the sheet is also the mid thickness. The obtained results are compared to study the efficiency of each technique in 1050 Al.

2. Methodology

For the present study, 1050 Al is chosen for its minimum solute content property (99.7 % Al) making it an ideal yet fundamental system to examine the dislocation evolution in aluminum alloys. The thickness reduction was performed using a laboratory rolling set up with a roll diameter of 150 mm. A reduction of 46.8 % was obtained by a single pass employing a non-lubricated symmetric rolling procedure. Prior to the cold rolling experiment, the sample was annealed at 550 °C to reduce the internal stress associated with the thermomechanical processes (TMP) during manufacturing.

The rolled samples were mechanically grinded and polished with Struers®-type DiaDuo suspensions containing one and three micrometer diamond particles. The hardness testing experiment was performed using Zwick/Roell® ZHVμ-type Vickers microhardness tester. The sample was studied about its transverse direction (TD) plane by making diamond shaped indents on the studied plane and capturing their hardness response.

After reduction, the final thickness of the sample was 1044.50 μm and the half of the thickness was defined as 522.25 μm. In the current analysis the area of study is in the region of 348μm to 522.25 μm, which is considered as the mid-thickness (core) of the rolled sheet. The indents were made with care to avoid overlapping of the deformation zones, induced by indentation in the corresponding points.

3. Results

3.1. Indentation Technique

On the studied area, indents were imposed on the polished surface by employing various loads, ranging from 10gf to 500 gf. However, for the calculation of total dislocation density, hardness values with very high deviation were neglected to avoid the so-called indentation size effect (ISE), which induces high hardness response at lower loadings [9]. For the current study, the hardness response from 200 gf to 500 gf were taken into consideration, which falls into saturation zone of the ISE curve [4].

In equation (1), the geometric constant α is generally considered to be a constant value for a wide range of straining, however, to ensure more accurate assessment of dislocation density, this parameter was calculated using the following equation [4]:

$$\alpha \cong \frac{(1 - 0.5\nu)}{4\pi(1 - \nu)} ln\left(\frac{\rho^{-0.5}}{b}\right) \quad (5)$$

where ν = 0,35 is the Poisson ratio for Al.

The constant α has been calculated by equation (5) via defining ρ for varies strain ε values using equation (4). From the approximated $\rho(\varepsilon)$ values α is presented for a wide range of reductions in Figure 1. From the variation of α with strain, it has been reported that the value of geometric constant tends to saturate at ~ 0.5 as the amount of strain increases. The value of α is 0.5756 for the sample deformed with a true strain of 0.63 as per Figure 1.

The Taylor factor M (see Table 1) was recorded by texture maps obtained from the electron backscattering diffraction (EBSD) experiments. The Burgers vector b and shear modulus G for aluminum alloys are 0.2865 nm and 26 GPa, respectively. The final dislocation density value calculated by equation (1) is 1.7 × 10^{14} m^{-2}. The calculation details are presented in Table 1.

3.2. Numerical Models

In the numerical approach developed by Kubin and Estrin [6] the modelling parameters C_1, C_2, C_3 and C_4 are defined for aluminum alloys and given as: C_1 = 2.33×10^{14} m^{-2}, C_2 = 1.1, C_3 = 4 × 10^5 1/m, C_4 = 1.2 [8]. The dislocation density is calculated for aluminum alloys by both K-E and modified K-E

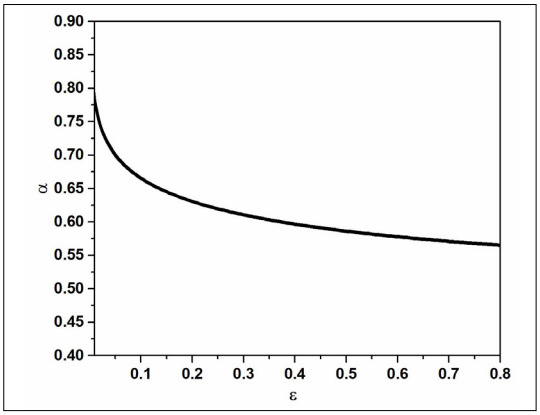

Figure 1. *Variation of α with strain predicted by eq.*

Table 1. *Evaluation of dislocation density by indentation technique data*

ε	α	M	Average HV (Pa)	ρ (m^{-2})
0.63	0.5756	3.16	4.11×10^{8}	1.7×10^{14} ±0.06

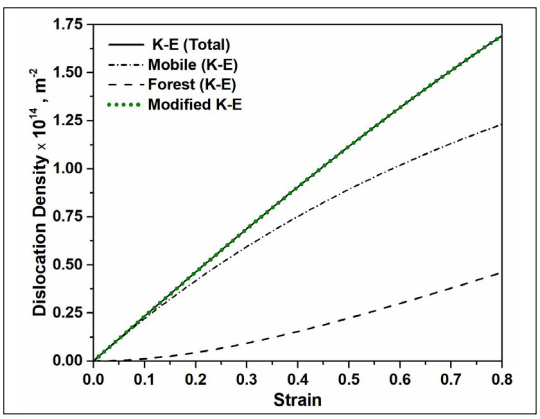

Figure 2. *Evolution of dislocation density predicted by the K–E* ***[6]*** *and modified* ***[7]*** *models over a range of strain.*

Table 2. *Dislocation density ($\rho \times 10^{14}$ m^{-2}) calculated by three techniques*

ε	Indentation	K–E	Modified K–E
0.63	1.7±0.06	1.4	1.4

technique using equations (2) to (4) for various straining level, which is represented in **Figure 2.**

Analyzing **Figure 2** it becomes obvious that the *ρ(ε)* obtained by the K-E and simplified K-E methods are nearly identical, however, employing K-E technique one can evaluate the contribution of forest and mobile dislocations. The total dislocation density is found to be dominated by the amount of mobile dislocations over the range of strain as shown in **Figure 2.** The same is true for the respective strain of $\varepsilon = 0.63$.

The calculated values of dislocation density by the three techniques are represented in **Table 2**.

Table 2 shows that the dislocation density results obtained from both K-E and modified K-E is exactly same for the mid thickness layer of 46.8 % deformed 1050 Al, however, results obtained from the indentation method are slightly higher than the model predictions. This discrepancy can be explained by the presence of solutes in the investigated Al alloy, which additionally contributes to the hardening and therefore, the value of hardness in the investigated alloy is somewhat higher compared to pure Al. Another possible reason why the numerical approach provides slightly lower value is the complexity of dislocation interactions during deformation, which cannot be fully captured by the models employed.

4. Conclusion

Results of the current investigation clearly demonstrate that microindentation is capable of providing reasonable values of dislocation density, which tend to evolve during plastic deformation. The estimated dislocation density in 1050 Al alloy is in a good agreement with the theoretically assessed counterparts. The indentation technique makes possible to investigate the distribution of dislocation density across the thickness of deformed materials.

The Kubin-Estrin method can successfully provide a good approximation of the amount of mobile and forest dislocations responsible for work hardening at various levels of straining. On the other hand, modified K-E is a very simple and efficient approximation of the dislocation density. It has been shown that the modelling techniques employed slightly underestimate the density of dislocations most probably due to the complexity of dislocation interactions, which cannot be captured by these numerical approaches.

Acknowledgment

This research was carried out within project no. TKP2021-NVA-29. The financial support is provided by the Ministry of Innovation and Technology of Hungary from the National Research, Development, and Innovation Fund. The work is financed under the TKP2021-NVA funding scheme.

References

[1] Humphreys F. J., Humphreys F. J., Rohrer G. S., Rollett A. D., Rollett A. D.: *Recrystallization and related annealing phenomena*, Third edition. Amsterdam Oxford Cambridge, MA: Elsevier, 2017.

[2] Callister W. D., Callister W. D.: *Fundamentals of materials science and engineering: an interactive etext*. New York: Wiley, 2001.

[3] Csontos A. A., Starke E. A.: *The effect of inhomogeneous plastic deformation on the ductility and fracture behavior of age hardenable aluminium alloys*. International Journal of Plasticity, 21/6. (2005) 1097–1118. https://doi.org/10.1016/j.ijplas.2004.03.003

[4] Sidor J. J., Chakravarty P., Bátorfi J. Gy., Nagy P., Xie Q., Gubicza J.: *Assessment of Dislocation Density by Various Techniques in Cold Rolled 1050 Aluminum Alloy*. Metals, 11/10. (2021) 1571. https://doi.org/10.3390/met11101571

[5] Taheri M., Weiland H., Rollett A.: *A method of measuring stored energy macroscopically using statistically stored dislocations in commercial purity aluminum.* Metallurgical and Materials Transactions A, 37/1. (2006) 19–25. https://doi.org/10.1007/s11661-006-0148-1

[6] Kubin L. P., Estrin Y.: *Evolution of dislocation densities and the critical conditions for the Portevin-Le Châtelier effect.* Acta metallurgica et materialia, 38/5. (1990) 697–708. https://doi.org/10.1016/0956-7151(90)90021-8

[7] Csanádi T., Chinh N. Q., Gubicza J., Langdon T. G.: *Plastic behavior of fcc metals over a wide range of strain: Macroscopic and microscopic descriptions and their relationship*. Acta Materialia, 59/6. (2011) 2385–2391. https://doi.org/10.1016/j.actamat.2010.12.034

[8] Csanádi T., Chinh N. Q., Gubicza J., Vörös G., Langdon T. G.: *Characterization of stress–strain relationships in Al over a wide range of testing temperatures.* International Journal of Plasticity, 54. (2014) 178–192. https://doi.org/10.1016/j.ijplas.2013.08.014

[9] Nix W. D., Gao H.: *Indentation size effects in crystalline materials: A law for strain gradient plasticity.* Journal of the Mechanics and Physics of Solids, 46/3. (1998) 411–425. https://doi.org/10.1016/S0022-5096(97)00086-0

sciendo

Acta Materialia Transylvanica 5/1. (2022) 10–13.
DOI: Hungarian: https://doi.org/10.33923/amt-2022-01-03
English: https://doi.org/10.33924/amt-2022-01-03

ACTA MATERIALIA TRANSYLVANICA

Laser Cutting of Brass Sheet

Enikő Réka FÁBIÁN,[1] Bence CZIGÁNY[2]

[1] *Óbuda University, Bánki Donát Faculty of Mechanical and Safety Engineering Faculty, Institute of Materials and Manufacturing Sciences, Material Science and Deformation Engineering Department, Budapest, Hungary, fabian.reka@bgk.uni-obuda.hu*

[2] *Bay Zoltán Nonprofit Ltd. for Applied Research, Production Division, Department of Production Development, Budapest, Hungary, czbence997@gmail.com*

Abstract

Laser cutting of copper-based alloy sheets is very difficult due to their high reflectivity, which can be modified with graphitization. The optimal parameters for a 2.5 mm thick brass sheet were determined by examining the laser beam parameter variations and the laser cut kerfs. The best characteristics of kerfs were obtained when the surface was graphitized, the laser frequency was 200 Hz, the applied laser speed was 1400 mm/min on 2500 W power and the focal point was under the surface by 0.8 mm. The applied working gas was nitrogen.

Keywords*: brass, laser cutting, kerf.*

1. Introduction

Among laser technologies used at the present time in machine-building industries, gas laser cutting of metallic and non-metallic materials has become widely used [1-5]. Laser offers considerable advantages over conventional techniques due to precision of operation, short processing time, and low cost. The physical processes involved in laser cutting of thick sections are complicated and significantly influence the end product quality. Laser parameters - in particular laser output power, focus on setting of focusing lens, cutting speed, assisting gas, and its pressure - influence the physical processes in the cutting section [6, 7]. Controlling the affecting parameters results in improved cutting quality. Consequently, investigation into affecting parameters in laser cutting process is necessary to improve the end product quality.

Laser cutting of carbon and stainless steels is well studied even in the case of thick sheets [8, 9]. The kerf width variation during CO_2 laser cutting was investigated by Uslan [9], who showed the variation in laser power intensity resulted in considerable variation in the kerf width size during the cutting process, being more pronounced at lower intensities. According to the literature [10] in the case of austenitic stainless steels, the size of the heat affected zone increases with increased workpiece thickness. In these steels the laser pulse frequency has a notable effect on the cut quality; however, this effect is not in a linear form with the kerf size and dross height [10]. Cutting metals of the copper alloys group is difficult due to the high thermal conductivity of the material and large coefficient of heat capacity. The high reflectivity of copper alloys imposes certain requirements on the equipment. In preparation for the process, it should be taken in consideration that the laser cutting of copper is more difficult the thicker the plate [11, 12]. After Daurellio et al. [12] the laser welding of copper sheets is possible by overlapping layers of cupric oxide, CuO, with a small quantity of cuprous oxide, Cu_2O grown under laser beam irradiation. This experimental approach, to increase the copper surface absorption of the laser radiation [12] can be applied at cutting also. The reflectivity of copper and other reflective metals decreases when the metal warms up, and drops sharply once the material melts [13]. According to the literature, the maximum cutting speed is achieved if the focal plane of the beam is positioned at the plate

surface for thin sheets, or about one third of the plate thickness below the surface for thick plate [6]. Distance of focus position is the distance from the focal point to the upper surface of the cutting workpiece. The position of the focal point above the workpiece is generally called the positive focal point, the position of the focal point below the workpiece is generally called the negative focal point. The kerf width depends on the focal position [13, 14]. Changing the focus position means changing the spot size on the surface and inside of the board. The focus length becomes larger, the spot becomes thicker, and the slit becomes increasingly wider, which in turn affects the heating area, slit size, and slag discharge capacity.

When piercing and cutting copper, high-pressure oxygen is typically used as the cutting gas to increase process reliability. When oxygen is used, the formation of copper oxide on the surface reduces the reflectivity. For brass, nitrogen cutting gas works fine [13]. As an approximate guide to setting the power, the literature gives different minimum required peak powers for different copper plate thicknesses [13].

2. Materials and testing

As part of the experiment, cutting of copper alloy sheet by Trump TLF 5000 turbo CO_2 gas laser equipment was performed. The effect of varying frequency and cutting speed on the cut slit were monitored. The focal positions applied were –0.8 mm, and –2 mm. Based on the literature [13] the applied power was 2500 W. Some parameters were also tested on graphitized surfaces, which reduces the surface reflection.

During the cutting experiments, the process settings were modified after visual inspection. For light and electron microscopical studies Neophot 2 and Olympus DSX light microscopes were used. The studied sheet was a brass with ~34 % zinc, with 2.5mm thickness.

The kerfs-shape and microstructure near the cut edges were studied on metallographic prepared transverse sections, cut at 25 mm from the laser cutting lines ends, in polished and etched condition. The etchant used was 10 % solution of ammonium-peroxo-disulphate. The laser cutting parameters are shown in Table 1.

If the energy input proved insufficient, the molten brass flowed back to the plate surface.

Table 1. *The cutting parameters*

Nr.	f (Hz)	v (mm/min)	Focus (mm)	Graphite	Success
1	600	2250	–0.8	no	no
2	600	2000	–0.8	no	no
3	600	1800	–0.8	no	no
4	600	1600	–0.8	no	no
5	600	1400	–0.8	no	partial
6	200	1400	–0.8	no	partial
7	200	1400	–2	no	no
8	200	1400	–0.8	yes	yes
9	200	1600	–0.8	yes	no
10	200	1200	–0.8	yes	yes
11	200	1500	–0.8	yes	no
12	200	1000	–0.8	yes	yes

3. Results

By visual inspection (Figure 1) it was observed that at a cutting speed of more than 1400 mm/min, the 2.5 mm brass plate is not cut through the full plate thickness, molten material appearing on the surface of the plate. Slit appearance on the bottom part of sheet in the case of a 1400 mm/min cutting speed depended on the other parameters. Applying the focal spot on the bottom side of the sheet (cut nr. 7), with similar parameters

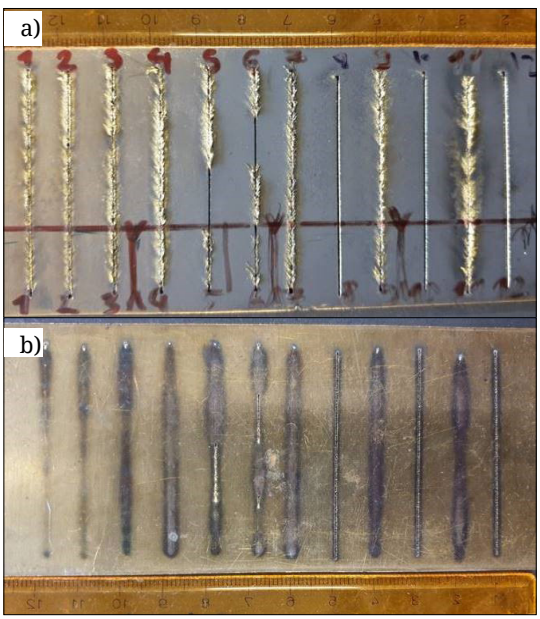

Figure 1. *The laser parameter effects at d = 2.5 mm sheet, P = 2500 W. a) crown face b) root face*

as cutting line 6 (f=200 Hz, v=1400 mm/min) a large amount of melted material came back on the surface. Cutting a gap through the full plate thickness was possible at 1000-1400 mm/min cutting speed when the focal spot was at 1/3 part of sheet thickness (**Figures 1–2**), and the reflection was reduced by graphite paint.

On the transversal section it can be seen that the melted zone became bigger as the cutting speed decreased (**Figure 2**) Studying the metallographic prepared samples after etching, it became visible that the melted material, and the slag remain inside of the slit when the frequency was high, even if 1400 m/min speed was applied (**Figures 2–3**).

The frequency reduction gives smaller quantity remnant material on the slit surface after cutting (**Figures 3–4**).

Regarding the cutting of graphitized brass sheet, a smaller quantity of remelted material was observed on the cut edge (**Figure 4**), and for this reason the roughness at this surface is smaller (**Figure 4.** c, d).

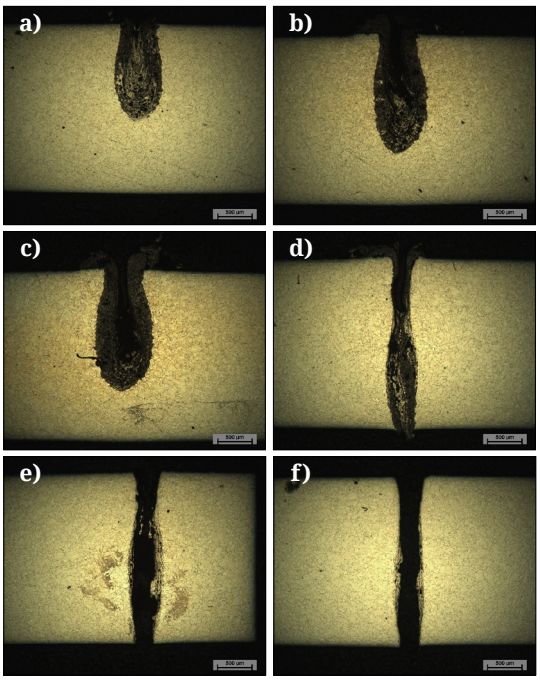

Figure 2. *The kerf appearance. on metallographic samples, at P=2500 W and f_p=−0.8 mm*
a) f = 600 Hz, v = 2000 mm/min,
b) f = 600 Hz, v = 1800 mm/min,
c) f = 600 Hz, v = 1600 mm/min,
d) f = 600 Hz, v = 1400 mm/min,
e) f = 200 Hz, v = 1400 mm/min,
f) f = 200 Hz, v = 1400 mm/min, graphitized.

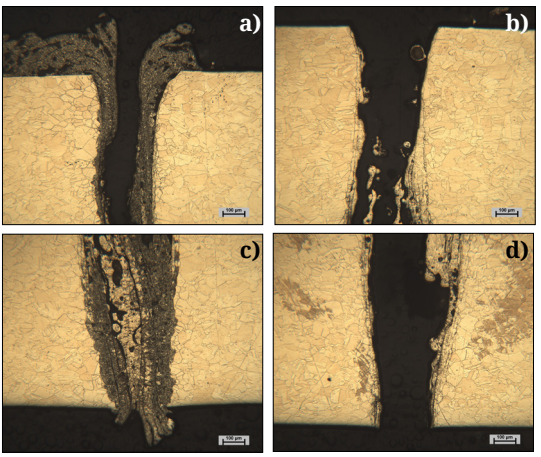

Figure 3. *Frequency effect on the remnant material in cutting gap, v = 1400 mm/min, f_p = –0,8 mm, no graphite*
(a, c) f = 600 Hz
(b, d) f = 200 Hz

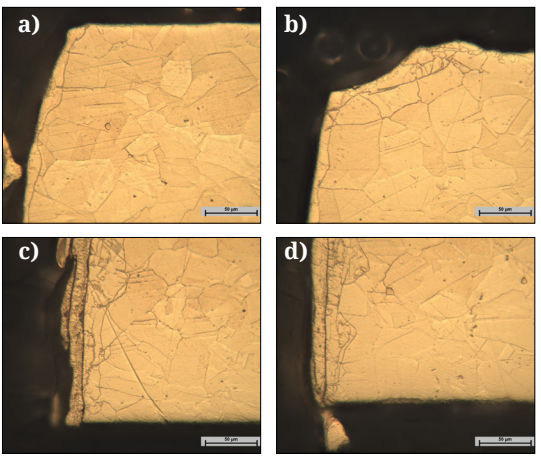

Figure 4. *Melted zone appearance on the cut edge P=2500 W, v=1400 mm/min, f_p =−0.8 mm f=200 Hz*
(a, c) no graphite,
(b, d), graphitized

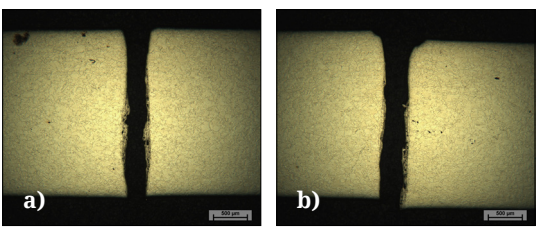

Figure 5. *Cutting speed effect on the cut slit, f_p =−0.8 mm, f=200 Hz,*
a) v=1400 mm/min
b) v=1000 mm/min

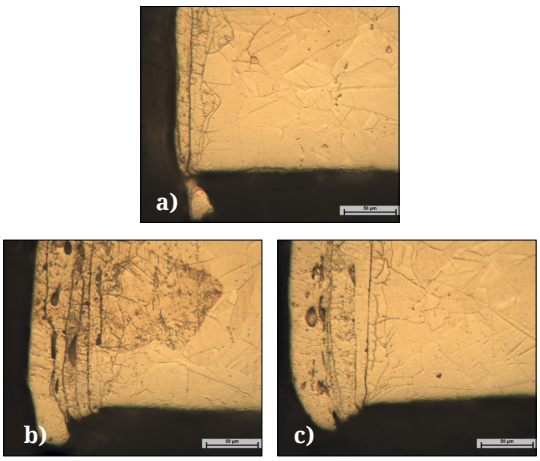

Figure 6. *Cutting speed effect on the cut slit*
f_p *= –0,8 mm f = 200 Hz*
a) v = 1400 mm/min
b) v = 1200 mm/min
c) v = 1000 mm/min

Decreasing the cutting speed, the cut slit became wider, but more parallel (**Figure 5**), on the cut edge more remelted material remained (**Figure 6**).

4. Conclusion

Cutting a gap through the full plate thickness was possible at 2500 W, when the cutting speed was 1000-1400 mm/min and when the focal plane was at –0.8 mm and the frequency was 200 Hz. The beneficial effect of graphite painting, in addition to protecting the laser equipment by reducing the strong light reflection, was also observed in the cutting-edge roughness.

Acknowledgements

The authors would like to thank the Hungarian State, the National Research, Development and Innovation Office and the European Union for their support in project No. 2020-1.1.2-PIACI-KFI-2020-00081.

References

[1] Astashchenko V. I., Zapadnova N. N., Mukhametzianova G. F., Shafigullina A. N.: *Key concepts for production of high-quality parts.* IOP Conference Series: Materials Science and Engineering, 240. (2017), v No 012007. https://doi.org/10.1088/1757-899X/240/1/012007

[2] Teregulov N. G., Sokolov B. K., Matveeva V. S.: *Quality of the processed surface during laser cutting and its control.* Kumertau Aviation Industrial Enterprise Institute, 2007.

[3] Ronald D. Schaeffer: *Fundamentals of Laser Micromachining*. CRC Press. USA, 2012. 25.

[4] John Powell: *CO_2 Laser Cutting*. Springer. USA, 1993.

[5] Narendra B. Dahotre, Sandip P. Harimkar: *Laser Fabrication and Machining of Materials*. Springer. USA, 2008. 193–196.

[6] Ion J.: *Laser Processing of Engineering Materials*: *Principles. Procedure and Industrial Application* eBook ISBN: 9780080492803. 2005. 347–369.

[7] Bahman Zohuri: *Thermal Effects of High Power Laser Energy on Materials*. Springer. USA, 2016. 1.

[8] Yilbas B. S.: *Laser cutting of thick sheet metals: Effects of cutting parameters on kerf size variations.* Journal of Materials Processing Technology (2008) 285–290. https://doi.org/10.1016/j.jmatprotec.2007.11.265

[9] Uslan I.: *CO_2 laser cutting: kerf width variation during cutting*. Proceedings of the Institution of Mechanical Engineers, Part B: Journal of Engineering Manufacture, 219. (2005) 571–577. https://doi.org/10.1243/095440505X32508

[10] Keles O., Oner U.: *Laser Cutting Process: Influence of Workpiece Thickness and Laser Pulse Frequency on the Cut Quality*. Arabian Journal for Science and Engineering volume, 37. (2012) 2277–2286. https://doi.org/10.1007/s13369-012-0306-2

[11] Daurelio G., M. Dell' Erba, Cento L.: *Cutting Copper Sheets by CO_2 laser*. Lasers & Applications, 5/3. (1986) 59–64.

[12] Daurelio G., M. Giorelo G.: *Experimental techniques to cut and weld copper by laser. A review*. Materials and Manufacturing Processes, 6/4. (1991) 577-603. https://doi.org/10.1080/10426919108934791

[13] Valentin P. Gapontsev: *How to Laser Cut Copper and Other Reflective Metals*. Ph.D thesis, EU, 2021. https://lasersystems.ipgphotonics.com/ resources/blog/how-to-laser-cut-copper-and-other-reflective-metal

[14] The focal point position effect on split. https://www.xtlaser.com/optimal-laser-equipment-bunny

sciendo

Acta Materialia Transylvanica 5/1. (2022) 14–17.
DOI: Hungarian: https://doi.org/10.33923/amt-2022-01-04
English: https://doi.org/10.33924/amt-2022-01-04

ACTA MATERIALIA TRANSYLVANICA

Selection Method of Flow Modifier Polymers for Chemical Enhanced Oil Recovery

Máté HARTYÁNYI,[1] Roland NAGY,[2] László BARTHA,[3] Sándor PUSKÁS[4]

[1] *University of Pannonia, Veszprém, Hungary, hartyanyi.mate@mk.uni-pannon.hu*
[2] *University of Pannonia, Veszprém, Hungary, , nroland@almos.uni-pannon.hu*
[3] *University of Pannonia, Veszprém, Hungary, , bartha@almos.uni-pannon.hu*
[4] *MOL Nyrt, Algyő, Hungary, spuskas@mol.hu*

Abstract

Chemically enhanced oil recovery methods can provide a solution to increase oil recovery. Of these, surfactant- polymer flooding is common. Efficient selection of polymers and surfactants is essential for a successful EOR project. Detailed selection of polymers is a lengthy task that involves a number of studies. Our goal is to create a fast polymer selection method based on which the most promising polymer can be selected.

Keywords: *polymer selection, dynamic viscosity, hydrodynamic diameter, enhanced oil recovery.*

1. Introduction

Enhanced oil recovery methods are often used to enhance crude oil recovery. [1]. Among the tertiary oil recovery methods, the use of water-soluble polymers is widespread. Oil yield can be enhanced with the increased viscosity of the water phase by the use of polymers. [2, 3]. This method is often used together with surfactant flooding Besides, for a successful EOR project efficient selection of the polymers and surfactants is essential [4]. Many variants of the polymers used for these purposes are known. Polymer manufacturers generally make suggestions for polymer products that can be potentially used, but their number is still numerous. [5, 6]. Their selection is a long task involving a number of studies [7, 8]. At the end of this process, the most efficient polymers are selected, with which the selection of surfactants can be continued.

Our goal was to create a fast polymer selection method that can be used to select the polymer products that are expected to be the most suitable for the purpose and based on this, the selection of surfactants can be started before the more detailed polymer selection procedure is completed. Nevertheless, it is not the aim to omit the full testing procedure of polymers.

2. Materials

For the experiments, the various viscosity-increasing polymers (Section 2.2) were dissolved in synthetically prepared model brine (Section 2.1). The polymers were added to the brine at a concentration of 1 g/L, and the solutions were stirred in a closed vessel at laboratory temperature for 8 hours using a magnetic stirrer. After the stirring time, the solutions were stored overnight.

2.1. Brine

Synthetic brine, freshly prepared before use, was utilized for the experiments. The composition of this synthetic brine is shown in Table 1.

Table 1. *Used salts for prepared synthetic brine*

Used salt	Concentration, g/L
NaCl	0.5
$CaCl_2$	0.2
$NaHCO_3$	2.6
CH_3COONa	2.6
Sum	5.9

Each of the salts which was used in the assays is an anhydrous analytical grade chemical.

2.2. Polymers and its solutions

In our work, aqueous solutions of synthetic copolymers from polyacrylamide and acrylonitrile tertiary-butyl sulfonate were investigated. Furthermore, the mentioned compounds had similar molecular structure which are commonly used in practice. The tested polymers were available in granulated form. The most important properties are summarized in **Table 2.**

Table 2. *The investigated polymers and their properties* **[9]**

Type of polymer	Average molecular weight	Anionicity
FP AN125VLM	very low	medium
FP AN125	medium	medium
FP AN125SH	high	medium
FP AN125VHM	very high	medium

There was a difference in the average molecular weight of the used polymers.

3. Product analysis

In order to characterize the polymer solutions, their solubility was investigated, also, the dynamic viscosity was measured and the hydrodynamic permeability was determined.

3.1. Examination of solubility

Solubility was examined visually. In order to be able to assign a physical amount, the light transmittance (transmittance) of the solution was measured spectrophotometrically with an Avantes spectrophotometer. The tests were performed with light at a wavelength of 520 nm and taken as 100 % when the light was completely transmitted by the solution and 0 % when the irradiated light did not pass through the solution in the 1 cm measuring cell.

3.2. Viscosity

In our experiments we used an automatic viscometer of the SVM 3000 Stabinger Viscometer type manufactured by Anton Paar to measure the dynamic viscosity of the solutions. Viscosity is measured on a rotating basis. The device performs the tests at a constant shear rate of 100 1/s and determines the dynamic viscosity.

3.3. Determination of hydrodynamic diameter

In our experiments, a Malvern Nano ZS instrument was used to measure the hydrodynamic diameter of the polymer in solution. Measurements were performed at 25 °C.

4. Results

The measurement results of solubility of the polymers are summarized in Section 4.1, the data of the hydrodynamic diameter tests in Section 4.2 while the dynamic viscosity data are summarized in Section 4.3.

4.1. Solubility of polymers

The solubility of polymers is one of the key criteria for their applicability, so this property was considered a selection condition. Polymers that were not completely soluble were excluded from further studies. The results are summarized in **Table 3.**

Table 3. *The solubility of used polymers during the analysis*

Type of polymer	Transmittance, %	Attendance
FP AN125VLM	100	transparent
FP AN125	100	transparent
FP AN125SH	100	transparent
FP AN125VHM	100	transparent

All of the polymers tested were dissolved in the used brine. No turbidity or precipitation was observed and all of them were found to be suitable for further investigation

4.2. Dynamic viscosity of polymer solutions

The dynamic viscosity data of the polymer solutions at 80 °C are summarized in **Table 4**.

Table 4. *Dynamic viscosity of polymers at 80 °C*

Type of polymer	Dynamic viscosity (80 °C), mPa·s	Ranking
FP AN125VLM	1.58	-
FP AN125	2.52	3
FP AN125SH	2.88	2
FP AN125VHM	4.09	1

Based on the values measured at 80 °C, the highest dynamic viscosity was considered the best result. Furthermore, it was determined as a condition that the dynamic viscosity of the polymer solution be higher than the value of the crude oil measured at 80 °C, which is 2.43 mPa·s. Based on the latter, FP AN125VLM did not meet the criterion.

4.3. Hydrodynamic diameter of polymers

The test results for the hydrodynamic diameter of the polymers in solution are summarized in **Table 5**.

Table 5. *Hydrodynamic diameter of polymers*

Type of polymer	Hydrodynamic diameter, nm
FP AN125	385.9
FP AN125SH	420.8
FP AN125VHM	777.7

The solution of polymers injected into the reservoir must pass through the porous rock. The hydrodynamic diameter of polymers in solution has been the subject of a number of studies on the relationship between the pore throat of a petroleum reservoir rock and polymer filtration**[10]**. Oort et al. **[11]** were the first to formulate the "1/3: 1/7 rule", according to which if the hydrodynamic diameter of the polymer exceeds 1/7 of the diameter of the pore pores, it will become trapped in the pores and lead to polymer loss. In the case of the oil field where the tests were based, the average pore throat diameter was 5 μm. Therefore, the maximum hydrodynamic diameter was taken to be 714.2 nm and the polymer for which this value was higher (FP AN125VHM) was excluded from the test series.

5. Conclusion

At first, solubility was examined in the study of polymers. Based on this, all of the polymers met the requirements. Subsequently, the dynamic viscosity data of the solutions were examined, where the criteria was that the dynamic viscosity of the polymer solution should be higher than the dynamic viscosity of the crude oil. The function of the polymers is to increase the dynamic viscosity, so a ranking was made based on the results. Afterwards, the hydrodynamic diameter of the polymers in solution was investigated, where the diameter of the average pore tube throat must be less than 1/7 . The tests and criteria are summarized in **Table 6.**

Table 6. *Experiments and criteria*

Experiment	Criteria
Solubility	Complete dissolution, transparent solution
Dynamic viscosity	Higher crude oil viscosity, maximum viscosity increasing effect
Hydrodynamic diameter	Smaller, than 1/7 pore throat diameter

Based on the criteria system, two polymers were found to be suitable at the end of the selection. These were polymers FP AN125 and FP AN125SH. Regarding the dynamic viscosity data, the latter is preferred. Displacement studies with these two polymers (using surfactants) were also performed at the Institute of Applied Earth Sciences of the University of Miskolc.

Table 7. *Displacement experiments of polymer-surfactants*

Type of polymer	Excess oil yield, %
FP AN125	26.6
FP AN125SH	31.9

In case of the polymer (FP AN125SH), it was also considered to be advantageous, a higher oil yield of more than 5 % was obtained.

The developed polymer selection method has been found to be suitable for making a preliminary quick decision on which polymer can be the most effective for cEOR purposes as well as for further studies with surfactants.

References

[1] Mohd T. T., Taib N. M., Adzmi A. F., Ab Lah N. N., Sauki A., Jaafar M. Z.: *Evaluation of polymer properties for potential selection in enhanced oil recovery.* Chemical Engineering Transactions, 65. (2018) 343–348. https://doi.org/10.3303/CET1865058

[2] Mandal A., Verman J.: *Potential effective criteria for selection of polymer in enhanced oil recovery.* Petroleum Science and Technology, 40/7. (2022) 879–892. https://doi.org/10.1080/10916466.2021.2007951

[3] Sorbie K. S.: *Polymer-improved oil recovery*. 1. kiadás. Springer Science & Business Media, New York, 1991. 1–4.

[4] Mahajan S., Yadav H., Rellegadla S. et al.: *Polymers for enhanced oil recovery: fundamentals and selection criteria revisited.* Applied Microbiology and Biotechnology, 105. (2021) 8073–8090. https://doi.org/10.1007/s00253-021-11618-y

[5] Shaw D. J.: *Introduction to colloid surface chemistry.* 4. kiadás Butterworths-Heineman, Oxford, 1992.

[6] McCormick C. L.: *Structural Design of Water-Soluble Copolymers*. In: Water-Soluble Polymers, ACS Symposium Series, Foreword: Synthesis, Solution Properties, and Applications. (Szerk.: Shalby W.S., McCormic C.L., Butler G.B.). American Chemical Society, Washington DC, 1991. 2–25.

[7] Levitt D., Pope G. A.: *Selection and screening of polymers for enhanced-oil recovery*. In: SPE symposium on improved oil recovery. Society of Petroleum Engineer, 2008, January.

[8] Rellegadla S., Prajapat G., Agrawal A: *Polymers for enhanced oil recovery: fundamentals and selection criteria.* Applied microbiology and biotechnology, 101/10. (2017) 4387–4402. https://doi.org/ 10.1007/s00253-017-8307-4

[9] https://www.snf.us/wp-content/uploads/2014/08/EOR-Oil-30-Years-of-EOR1.pdf (letöltve: 2020. október 18.).

[10] Guo Hu.: *How to select polymer molecular weight and concentration to avoid blocking in polymer flooding?* In: SPE Symposium: Production Enhancement and Cost Optimisation. Kuala Lumpur, Malaysia, 2017. https://doi.org/10.2118/189255-MS

[11] van Oort E., Van Velzen J. F. G., Leerlooijer K.: *Impairment by suspended solids invasion: testing and prediction.* SPE Production & Facilities, 8/3. (1993) 178–184. https://doi.org/10.2118/23822-PA

sciendo

Acta Materialia Transylvanica 5/1. (2022) 18–22.
DOI: Hungarian: https://doi.org/10.33923/amt-2022-01-05
English: https://doi.org/10.33924/amt-2022-01-05

ACTA MATERIALIA TRANSYLVANICA

Reinforced Matrix Syntactic Foams Filled with Ceramic Hollow Spheres

János Endre MARÓTI,[1, 2,a] Benedek SZOVÁK,[2,b] Imre Norbert ORBULOV[1,2,c]

[1] *MTA-BME Lendület Composite Research Group, Budapest, Hungary*

[2] *Budapest University of Technology and Economics, Faculty of Mechanical Engineering, Department of Materials Science and Engineering, Budapest, Hungary*

[a] *maroti.janos.endre@gpk.bme.hu,* [b] *szovak.benedek@edu.bme.hu,* [c] *orbulov.imre.norbert@gpk.bme.hu*

Abstract

Metal matrix syntactic foams are cellular materials in which the matrix is metal and within that matrix are non-metallic cells formed by filler material. These materials have low density, and besides that, they have high compressive strength and energy absorption. The main goal was to improve these properties by reinforcing the matrix with ceramic grains. During the experiment, molten A356 aluminium (7Si-0,3Mg) was infiltrated between the mixture of the filler and the reinforcement material. The specimens were produced with low-pressure infiltration. Different reinforcement materials were used: aluminium-oxide with three different grain sizes and colour designations and one type of silicon carbide. After heat-treatment, standardised compression tests were executed on the specimens. The results were compared to the results of the non-reinforced samples.

Keywords*: syntactic metal foam, reinforcement in matrix material, compression test.*

1. Introduction

Nowadays, porous, cellular materials are becoming more and more common in engineering applications, one of which is the subject of our research is metal foams. Their success is due to their low density, high specific energy absorption capacity, and strength.

Metal foams can be divided into two groups based on their structure, open and closed cell materials. The difference between the two groups, as their name suggests, is how separated the cells in the material are. In the case of closed-cell foams (**Figure 1**) the individual cavities are entirely separated from each other. In contrast, in the case of open-cell foams (**Figure 2**) there is no material boundary between the adjacent cells, the material-deficient areas meet.

As mentioned, metal foams have good specific mechanical properties in addition to their low

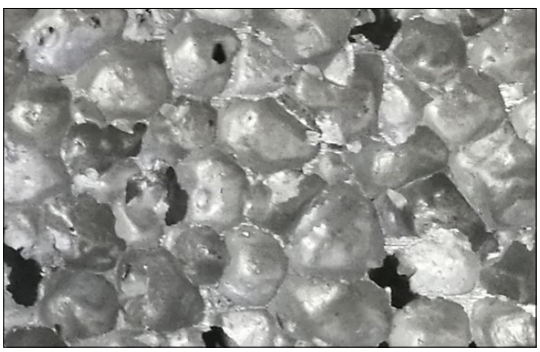

Figure 1. *Image of closed-cell metal foam.*

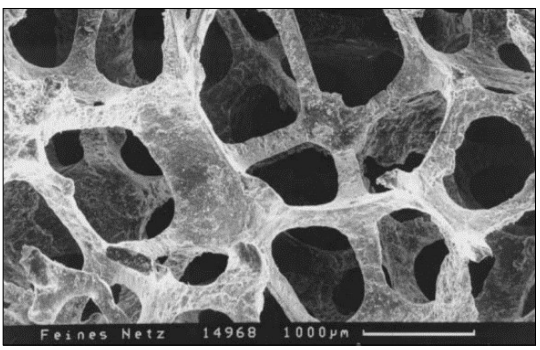

Figure 2. *Image of open-cell metal foam.* **[1]**

density. Several methods have been developed to improve these properties further and manipulate them for their intended application. These foams are referred to in the literature as functional metal foams, where the aim is to provide structural advantages in addition to the properties mentioned. Examples of these are the production of tubes filled with syntactic foam, which can withstand specifically bending stress [2], and varying the distribution and amount of filler in different parts of the foam according to function [3–5].

Furthermore, the size of the filler also has a significant effect on the mechanical properties. The strength properties can be variable by using different size fillers in the same material or mixing different filler materials [6–8]. In the case of non-reinforcing foams, this can be achieved by changing the manufacturing parameters [9].

The main goal of our research is the production and development of syntactic metal foams reinforced in their matrix material, and the investigating of their mechanical properties by quasi-static compaction testing.

Ceramic nano- and micro-particles have been successfully used in solid composites [10–12]. There is a chance that it is not possible to use a nano- or micro-sized reinforcement because the melt would press it to the bottom of the sample during infiltration. Nevertheless, based on the properties of the ceramic particles, we set up a hypothesis that a reinforcing material with a particle size in the 0.1-1 mm size range will also improve the tested mechanical properties.

2. Materials and methods

2.1. Materials

In our research, our matrix material was A356 aluminium alloy (7Si-0.3Mg). The filler material was a Glober® ceramic spherical shell sold by Hollomet GmbH. The ceramic spherical shells were aluminum-oxide marked with a typical diameter of 2.29 ± 0.16 mm [13, 14]. The hollow interior of the spherical shell will give the porosity of the metal foam. The reinforcing material was Al_2O_3 and SiC grains purchased from Granit Csiszolószerszámgyártó Kft. Stereomicroscopic images of the filler and reinforcing materials are shown in Figure 3. The nominal size of the reinforcing materials is known from the series of sieve sizes, which gives us an interval to determine the exact size of the reinforcing materials; it was measured on the microscopic images. The results are shown in Table 1.

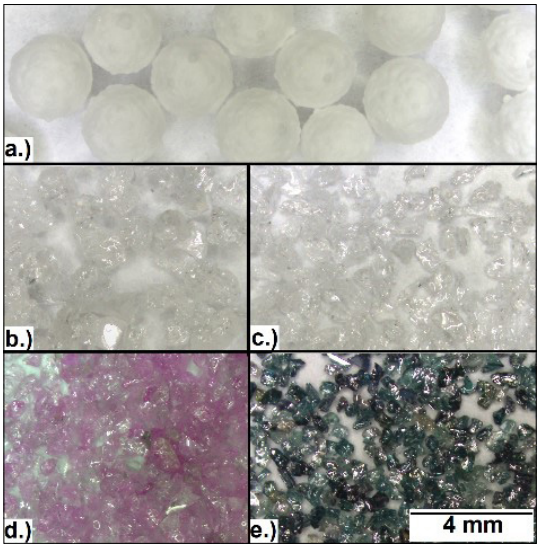

Figure 3. *Images of filler material (a), FS 18 Al_2O_3 (b), FS 40 Al_2O_3 (c), FS 46 Al_2O_3 (d), and FS 46 SiC (e) captured with stereomicroscope.*

Table 1. *Average particle size of reinforcing materials*

Reinforcing material	Nominal diameter (mm)	Measured diameter (mm)
FS 18 Al_2O_3	FS 18 (1 mm – 1.4 mm)	1.20±0.21
FS 40 Al_2O_3	FS 40 (0.4 mm – 0.7 mm)	0.63±0.09
FS 46 Al_2O_3	FS 46 (0.35 mm - 0.6 mm)	0.51±0.08
FS 46 SiC	FS 46 (0.35 mm - 0.6 mm)	0.45±0.09

2.2. Production of specimens

We used 20 wt% of the reinforcement for each case. The reinforcing material and the filler were mixed manually until it was visually determined that the reinforcing material was sufficiently distributed among the filler.

The inner surface of the used 40×50×240 mm enclosing molds was treated with graphite to facilitate casting removal using graphite spray. The degassing bore of the sample was sealed with aluminium-oxide paper, which allows air trapped during the casting to escape but prevents the melt from escaping.

After filling the mixture into the mold, a stainless-steel mesh was inserted atop the mixture. This was necessary because the density of the filler was lower than the melt, so it would float to the top and cause inhomogeneity problems. The molds were preheated for 1 hour at 600 °C in.

The A356 (7Si-0.3Mg) matrix material was melted in an induction furnace and heated to a low viscosity melt. After the furnace was turned off, the melt temperature was measured with a digital thermometer. After the temperature reached 840 °C, the melt was poured onto the top of the mixture. The gas inlet pipe was then placed on it, fixed in the gripping frame, and the argon gas was finally released at a pressure of 500 kPa. This squeezed the melt through our mixture.

The samples were air-cooled, and four specimens with an enclosure size of 30×30×40 mm and four specimens with 10 mm side length were processed from each block for quasi-static compression testing and microstructural examination.

Each sample was heat treated to increase strength. First, it was heated at 300 °C/h rate to 535 °C, held for 4 hours, then quenched in water. The second step involved heating at 200 °C/h rate to 150 °C, holding for 15 hours, then quenching in water [15].

2.3. Measurement methods

Samples for microstructural examination were grinded (with P60 - P4000 grind paper) and polished (by diamond suspension with a particle size of 3 μm and 1 μm) and then examined under optical microscopes.

The manufactured specimens' mechanical properties were investigated with a compression test based on ISO 13314: 2011 [16]. The quasi-static compaction test was performed on an MTS 810 universal electromechanical material testing machine. The device was equipped with a 250 kN load cell. Each specimen was compressed with a 4 mm/min cross-head speed to at least 50 % engineering strain value for comparability. To reduce friction, a 0.3 mm thick Kolofol Teflon foil was placed between the contact surfaces of the cross-head and the specimen.

Using the stress-strain data pairs, engineering stress-engineering strain curves were constructed in which the compressive strength (σ_c) was the first local maximum after elastic deformation, the plateau stress ($\sigma_{plateau}$) being the average stress in the range of 10 % to 40 % deformation, and the energy absorbed up to 50 % deformation (W_{50}), which is the area under the curve up to 50 % strain were examined (Figure 4).

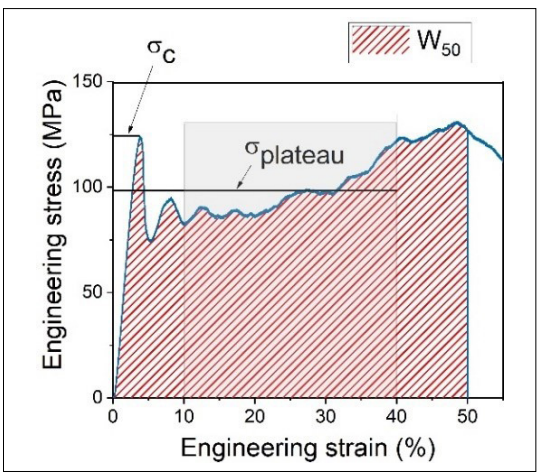

Figure 4. *Interpretation of tested mechanical properties.*

3. Results

The microstructural analysis indicated that the matrix developed a good connection with both the filler and the reinforcement material during infiltration, there was no considerable porosity or segregation on the boundaries of the filler or the reinforcement material. (Figure 5).

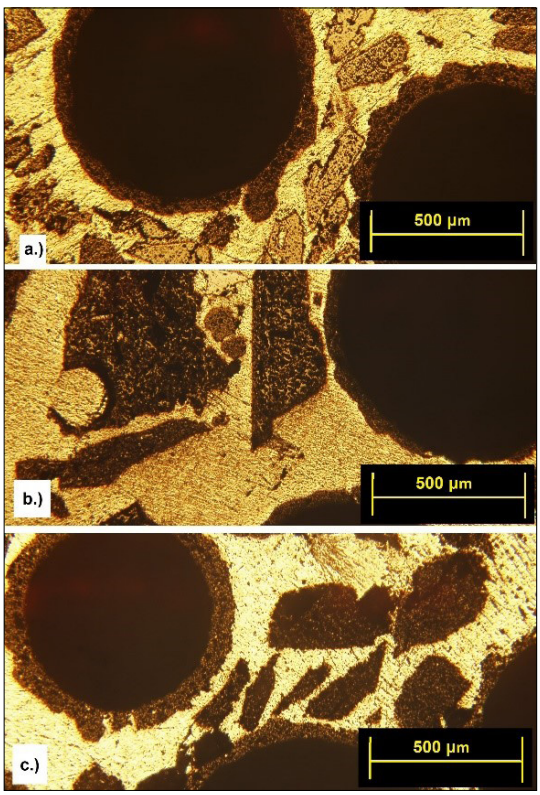

Figure 5. *Microstructure in the case of application of the FS 46 SiC (a), FS 18 Al_2O_3 (b) and FS 40 Al_2O_3 (c) reinforcement material (captured with an optical microscope).*

During the preparation of the specimens for microstructural analysis, we encountered the problem that due to the hardness of the filler- and the reinforcement material, the grains of the sanding paper were torn out, and scratched the already polished parts.

During the comperade of the results of the reinforced samples and the non-reinforced, it was shown that the reinforcement material always raised the compressive strength, but in the plateau region, the non-reinforced sample shows a monotone growing character, while some parts of the curve of the reinforced samples are monotone decreasing (**Figure 6**).

The results of the experiments are summarized in **Table 2.**

Table 2. *The examined mechanical properties*

Reinforcing material	Density (g/cm^3)	σ_c (MPa)	W_{50} (J/cm^3)
Non-reinforced	1.65±0.02	108.24±6.49	44.50±2.49
FS 46 SiC	1.78±0.06	124.94±4.61	39.50±4.65
FS 40 Al_2O_3	1.85±0.08	133.11±2.67	41.23±2.13
FS 46 Al_2O_3	1.79±0.08	116.42±9.83	36.42±4.20
FS 18 Al_2O_3	1.88±0.07	133.76±7.79	43.90±3.21

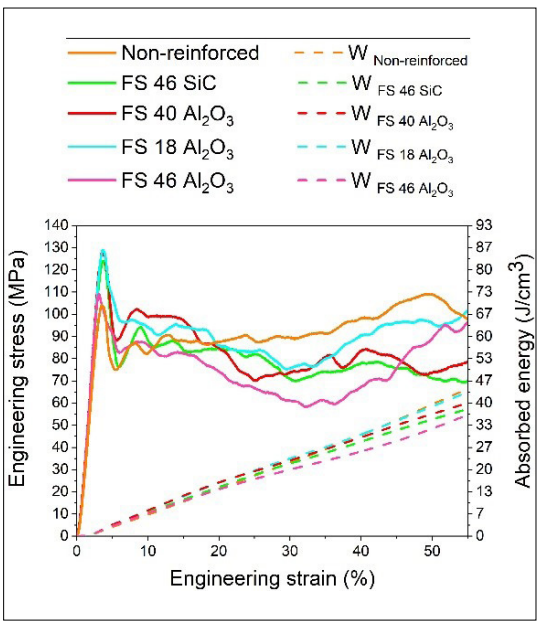

Figure 6. *The engineering stress-engineering strain curves and absorbed energy-strain curves of the different samples.*

4. Conclusions

From the results obtained during the research, we reached the following conclusions:

- Low pressure infiltration is an applicable method to produce syntactic metal foams reinforced in the matrix material, the reinforcement material is distributed to an appropriate extent evenly.
- There was an appropriate connection between the matrix and the filler and the matrix and the reinforcement material without porosity or segregations on grain boundaries.
- The usage of ceramic reinforcement is not always well-founded:
  - The ceramic filler material provides good mechanical properties.
  - The main benefit of reinforcement is the growth of compressive strength, it increases the compression strength by more than 17 % on average
  - From the reinforcement materials we used during the experiments the FS 18 Al_2O_3 was the best for application.

Acknowledgments

The research reported in this paper is part of project no. BME-NVA-02, implemented with the support provided by the Ministry of Innovation and Technology of Hungary from the National Research, Development and Innovation Fund, financed under the TKP2021 funding scheme, and the NRDI Fund (TKP2020 NC, Grant No. BME-NCS) based on the charter of bolster issued by the NRDI Office under the auspices of the Ministry for Innovation and Technology. This work was supported in part by the Hungarian Scientific Research Fund under Grant agreement OTKA FK_21 138505.

References

[1] J. Banhart: *Manufacture, characterization and application of cellular metals and metal foams*. Progress in Materials Science, 46/6. (2001) 559–632. https://doi.org/10.1016/S0079-6425(00)00002-5

[2] Kincses D. B., Károly D., Bukor Cs.: *Production and testing of syntactic metal foams with graded filler volume.* Materials Today: Proceedings, 45. (2021) 4225–4228. https://doi.org/10.1016/j.matpr.2020.12.163

[3] Kemény A., Leveles B., Kincses D. B., Károly D.: *Manufacturing and Investigation of In Situ and Ex Situ Produced Aluminum Matrix Foam-Filled Tubes*. Advanced Engineering Materials, 24/1. (2022) 2100365. https://doi.org/10.1002/adem.202100365

[4] Kincses D. B., Kemény A., Leveles B., Károly D.: *Csővel körülölelt fémhabalapú kompozitok gyártása, hőkezelése és vizsgálata*. Acta Materialia Transylvanica, 4/2. (2021) 93–96. https://doi.org/10.33923/amt-2021-02-07

[5] Movahedi N., Conway S., Belova I. V., Murch G. E., Fiedler T.: *Infuence of particle arrangement on the compression of functionally graded metal syntactic foams.* Materials Science and Engineering: A, 764. (2019) https://doi.org/10.1016/j.msea.2019.138242

[6] Kemény A., Leveles B., Bubonyi T., Orbulov I. N.: *Effect of particle size and volume ratio of hollow spheres on the mechanical properties of bimodal composite metal foams.* Composites Part A: Applied Science and Manufacturing, 140. (2021) https://doi.org/10.1016/j.compsitesa.2020.106152

[7] Orbulov I. N., Dobránszky J.: *Producing metal matrix syntactic foams by pressure infiltration.* Periodica Polytechnica Mechanical Engineering, 52/1. (2008) 35–42. https://doi.org/10.3311/pp.me.2008-1.06

[8] Muhammad A. N., Gábora A., Mankovits T.: *Influence of the Manufacturing Parameters on the Compressive Properties of Closed Cell Aluminium Foams*. Periodica Polytechnica Mechanical Engineering, 64/2. (2020) 172–178. https://doi.org/10.3311/PPme.16195

[9] Zamanai N. A. B. N., Iqbal A. K. M. A., Nuruzzaman D. M.: *Fabrication and characterization of Al_2O_3 nanoparticle reinforced aluminium matrix composite via powder metallurgy*. Materials Today: Proceedings, 29/1. (2020) 190–195. https://doi.org/10.1016/j.matpr.2020.05.541

[10] Sivananthan S., Ravi K., Samuel C. S. J.: *Effect of SiC particles reinfocement on mechanical properties of aluminium 6061 alloy processed using stir casting route*. Materials Today: Proceedings, 21/1. (2020), 968–970. https://doi.org/10.1016/j.matpr.2019.09.068

[11] Zaiemyekeh Z., Liaghata G. H., Ahmadi H., Khan M. K., Razmakhah O.: *Effect of strain rate on deformation behavior of aluminum matrix composites with Al_2O_3 nanoparticles.* Materials Science & Engineering: A, 753. (2019), 276–284. https://doi.org/10.1016/j.msea.2019.03.052

[12] Dhanashekar M., Loganathan P., Ayyanar S., Mohan S. R., Sathish T.: *Mechanical and wear behaviour of AA6061/SiC composites fabricated by powder metallurgy method.* Materials Today: Proceedings, 21/1. (2020), 1008–1012. https://doi.org/10.1016/j.matpr.2019.10.052

[13] ASM Handbook. Properties and Selection: Nonferrous Alloys and Special-Purpose Materials; ASM International: Materials Park, OH, USA, 1995.

[14] Szlancsik A., Katona B., Kemény A.: *On the Filler Materials of Metal Matrix Syntactic Foams*. Materials, 12/12. (2019), 2023. https://doi.org/10.3390/ma12122023

[15] Peng J., Tang X., He J. Xu D.: *Effect of heat treatment on microstructure and tensile properties of A356 alloys.* Trans. Nonferrous Met. Soc. China 21. (2011) 1950–1956. https://doi.org/10.1016/S1003-6326(11)60955-2

[16] ISO 13314:2011 – Mechanical testing of metals – Ductility testing – Compression test for porous and cellular metals. ISO133122011 – Mech. Test. Met. – Ductility Test. – Compression Test Porous Cell. Met. 2011.

sciendo

Acta Materialia Transylvanica 5/1. (2022) 23–28.
DOI: Hungarian: https://doi.org/10.33923/amt-2022-01-06
English: https://doi.org/10.33924/amt-2022-01-06

ACTA MATERIALIA TRANSYLVANICA

Investigation of the Application of Coagulants in case of Domestic Greywater Fraction

Zsófia MURGULY,[1] Ildikó BODNÁR[2]

University of Debrecen, Faculty of Engineering, Department of Environmental Engineering, Debrecen, Hungary

[1] *murgulyzsofia999@gmail.com*

[2] *bodnari@eng.unideb.hu*

Abstract

During our research work, we examined the removal of contaminants from synthetically produced bathing waters using different coagulants and studied the efficiency and the mechanism of coagulation-flocculation processes in detail. In our work, we performed experiments with two different types of coagulants (iron(III) chloride and polyelectrolyte) and compared their efficiencies. The zeta potential and its change were monitored as a qualifying parameter while other water quality parameters were also analyzed. In our experiments, a newly acquired flocculator device was also used to study the coagulation-flocculation processes of larger volume samples. The main goal of our research is to promote the sustainable management of drinking water quality and to study the bathing water reuse possibilities.

Keywords*: synthetic greywater, iron(III) chloride, polyelectrolyte, reuse.*

1. Introduction

According to the first point of the European Water Charter, “There is no life without water!”, that is, water as a living medium is vital. Ensuring the right quantity and quality of drinking water is a global problem today. Unfortunately, part of the world’s population does not have access to the daily amount of drinking water they need. It highlights the importance of managing the water, protecting this life-saving treasure from, e.g. the challenges of climate change. The so-called greywater fraction generated by various activities in households, such as washing dishes, showers, washing, cleaning, can be an effective alternative source, especially for activities that do not require drinking water quality, such as flushing toilets or even irrigation.

2. About greywater

In recent decades, especially in developing countries, the utilization of greywater has become the focus of attention as one of the solutions to water scarcity, and the utilization of this faction is still developing dynamically in the world. Greywater (GW) is the used water fraction in households that comes from washing dishes, bathing, washing, showering, washing hands, and washing clothes. That is the wastewater that is generated in the household and does not include the water used to flush the toilet. The literature classifies greywater fractions into two major groups: high pollutant greywater (HGW) and low pollutant greywater (LGW) fractions. The latter group includes mainly GW from bathrooms and hand washing. These mainly include soap, shampoo, body care products, as well as fats, oils, or even traces of faeces and urine that dissolve from human skin and hair during the cleansing process [1–3].

In Hungary, the daily water consumption per capita is around 97.8-100 L [4]. The GW can be approx. 65-70 % of the wastewater flow. Furthermore, the less loaded fraction (LGW) can represent 50 % of the total amount of GW. Based on all this, there is great potential for the reuse of these fractions. Based on the daily bathroom routine most of the GW is generated from showering, bathing, and handwashing, as one is cleaned in some form almost every day. Of course, its characteristics and amount also depend on several factors [3].

Our research focuses on the potential utilization of this GW fraction, during which we tried to reduce the amount of the main pollutants in this used water fraction by applying chemical water treatment. Iron(III) chloride and polyelectrolyte-type treatment agents were tested as coagulants. We studied the efficacy of the two agents and flocculation equipment was used to efficiently follow the flocculation processes.

3. Material and methodology

The tests of the greywater samples were performed in the Water Quality Protection Laboratory of the Department of Environmental Engineering, Faculty of Engineering, University of Debrecen. Based on the research results of the Water/Wastewater Utilization research group of the department, we prepared synthetic bathing water with a constant composition as model water. Our goal was to create and model the bath-water fraction by adding detergent components to the drinking water and to study the effects of different coagulants. Freshly prepared synthetic bathwater of the same composition was used for each series of tests.

To characterize the composition of the samples, the so-called non-specific physical and chemical parameters were determined. Measurements focused on determining pH, zeta potential, specific electrical conductivity, turbidity, biological oxygen demand (BOD5), total organic carbon (T/DOC), and anionactive detergent content. WTW SenTix 41-3 pH electrode for pH measurement, Zetasizer Nano Z device for zeta potential and specific electrical conductivity, OxiTop IS 12 for BOD_5 measuring, and Shimadzu TOC-VCPN device to measure total organic carbon were used. The ISO 2271: 1989 standard was applied to determine the anionactive detergent content of the samples [5–7].

The bathwater was prepared by adding 4 components (shower gel, shampoo, corn germ oil, and plant nutrient concentrate) dissolved in drinking water at 40 ˚C. As a first step in the chemical treatment, iron(III) chloride was used as a treatment agent during the coagulation, which was added to the water samples in different volumes in the form of a 25 gL^{-1} stock solution. 100 ml aliquots were pipetted into the beaker from the GW samples. The purpose of the treatment was to remove the non-settleable colloidal particles, and to convert dissolved pollutants into insoluble ones. We continuously measured the so-called zeta potential values and based on the measured values, the optimal amount of chemical was determined to achieve a zeta potential between 0±5 mV. During the measurement processes, a rapid stirring of 5 minutes was used for each sample portion, which facilitated the efficient mixing of the coagulants at 300 rpm. Thereafter, slow stirring for 15 min at 25-50 rpm was used to support the flocculation processes. Using a subsequent settling time of 10–15 min, efficient separation was achieved, and the zeta potential of the sample from the upper, clearer liquid layer was followed.

In our research, we also performed an examination with another treatment agent, this is a so-called polyelectrolyte treatment agent (ACEFLOC 80902). Similar to the previous treatment agent described above, the water samples were added in different volume units as a 1 g/l stock solution. To determine the optimal chemical dose, 100 mL aliquots of the synthetically prepared GW sample were also treated.

4. Conclusions

4.1. Greywater quality parameters

Based on the method given in the Materials and Methods section, the GW sample was prepared from 4 constituents (shower gel, shampoo, corn germ oil, and plant nutrient source). The results obtained during our work were compared with the results of previous literature and the research group of the Department of Environmental Engineering of the Faculty of Engineering of the University of Debrecen. The group determined the qualitative and quantitative parameters of the GW generated in households in the Northern Great Plain region. Thirty different households were selected for the survey, which included dwellings, townhouses, and single-family homes. Using this research and many other foreign works of literature, we were able to delimit the quality characteristics of bathing water samples [8].

Table 1 contains the quality parameters characteristic of bathing waters as GW fraction available in the international literature, the data determined by the research group, and the test results of the raw GW samples measured by us.

The composition of the synthetic bathing water prepared for our studies was clearly very similar to that of real bathing water sample quality. The pH of the bathing water used for our measurements is the same as the actual bathing water data measured in the region. Specific electrical conductivity and zeta potential values may vary,

Table 1. *Comparison of bathing water quality*

Parameters	International data [3]	National data [8]	Own results
pH	7.3–7.5	6.73–7.95	7.82±0.29
Specific electrical conductivity (mS/cm)	0.014–0.89	0.412–0.610	1.21±0.563
Zéta-potential (mV)	–	0.00–(–33.00)	–17.01±0.32
Turbidity NTU	84.8–375.0	2.3–84.0	21.49±15.28
BOI_5 (mg/L)	40.2–424	6.67–253.3	100.67±8.14
DOC (mg/L)	–	7.71–87.76	65.80±25.09
ANA-detergents (mg/L)	14.9–61*	0.01–4.18*	14.25±6.12

**MBAS parameter, parameter, which is very similar to ANA values but measured with a different measurement solution*

possibly due to the presence of different ions found in other brands of shampoo or shower gel. Variable contaminants, dead epithelial cells, and hair may affect the BOD_5, TOC, and turbidity values. We found that we were able to formulate synthetic bathing water with very similar quality to that determined in both the national and international literature.

4.2. Evaluation of treatments with ferric chloride

Table 2 shows the results of a series of 3 parallel treatments with ferric chloride, and **Figure 1** shows the change in zeta potential as a function of the amount of chemical added to show the success of the coagulation.

We have found that iron(III) chloride is an effective treatment agent, with the optimal amount of treatment agents ranging from 170 to 213 mg/L. Thus, the measured zeta potential value of 0 ± 5 mV was achieved. During the treatment process, flock formation was intense, and the use of a slow mixing step aided in efficient flocculation processes and better sedimentation properties of impurities.

The zeta-potential measurement confirmed that the initial very negative value moved in the positive direction in the coagulation-flocculation process, and in the ideal range of -5 mV to +5 mV the tested system will be proven to be destabilizing, i.e. contaminants can be settled from the water sample. The pH of the tested solutions varied with the amount of chemical added, as the chemical dose increased, the pH of the solution decreased, which meant that the samples produced acidic acidity. The turbidity values also showed a decreasing trend as we approached the optimal range, since if there is a sufficient amount of coagulant in a given greywater sample, using the appropriate settling time, visually purified, treated water is obtained. Conductivity data increased proportionally with the treatment agent overdose, similar to the turbidity value.

Table 2. *Treatment with ferric chloride in 100 mL bathwater sample aliquots*

	$FeCl_3$ volume (ml)	pH	Specific electrical conductivity (mS/cm)	Zeta-potential (mV)	Standard Deviation/ Zeta-potentiall	Turbidity (NTU)
1.	0.90	6.39	0.98	–8.38	0.295	9.07
	1.00	6.09	1.01	–0.70	0.156	7.67
	1.05	5.64	1.05	11.70	0.058	9.61
	1.15	5.81	1.05	12.10	0.407	19.45
2.	0.50	6.47	0.96	–10.2	0.416	4.75
	0.70	6.06	0.99	–4.56	0.133	3.09
	0.85	5.77	1.04	5.54	0.111	4.94
	0.90	5.55	1.03	2.91	0.745	5.33
	0.95	5.59	1.02	2.55	0.182	4.63
	1.00	5.43	1.06	8.76	0.322	5.25
	1.30	3.33	1.31	39.10	0.140	64.76
3.	0.50	6.48	0.95	–10.0	0.494	5.11
	0.70	6.09	0.99	–5.82	0.444	16.24
	0.80	6.02	0.98	–2.60	0.193	5.82
	0.90	5.44	1.04	12.10	0.404	7.51
	1.10	5.11	1.02	19.90	0.808	18.54

4.3. Evaluation of treatments with a polyelectrolyte type treatment agent

Table 3. summarizes the measurement results obtained from the 3 series of parallel treatments performed.

We found that the optimal dose for the polyelectrolyte (PE) type treatment agent was between 33-43 mg/L, that is, significantly less chemical is required to effectively treat 1 litre of synthetic bathwater.

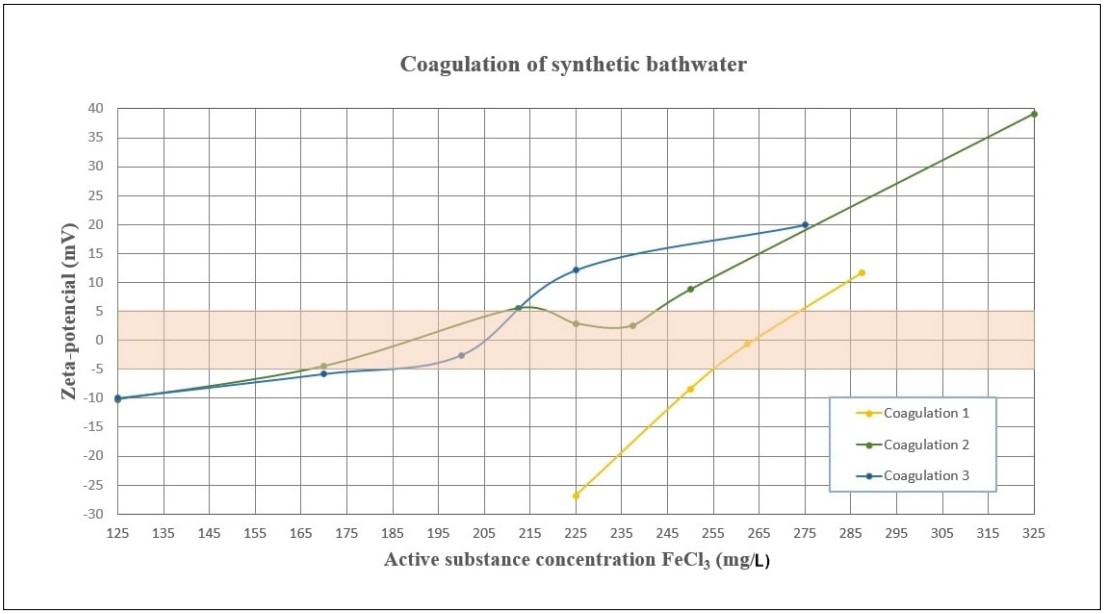

Figure 1. *Determination of the optimal amount of chemical in the case of ferric chloride.*

Table 3. *Coagulation with polyelectrolyte in 100 mL sample aliquots*

	PE volume (ml)	pH	Specific electrical conductivity (mS/cm)	Zéta-potential (mV)	Standard Deviation/ Zeta-potentia	Turbidity (NTU)
1.	0.50	8.35	0.85	–29.90	0.985	31.95
	1.00	8.43	0.84	–26.10	0.252	23.59
	1.25	8.40	0.86	–25.50	0.919	21.83
	1.50	8.39	0.86	–24.30	0.436	13.91
	5.00	8.36	0.78	26.10	0.819	31.50
2	2.00	8.34	0.85	–20.50	0.651	31.72
	3.00	8.31	0.83	–2.52	0.267	61.99
	3.30	8.25	0.80	3.60	1.500	71.30
	4.00	8.30	0.78	16.50	0.656	66.13
	5.00	8.31	0.81	29.10	0.379	79.73
3.	2.85	8.19	0.84	–19.40	0.351	8.87
	3.00	8.01	0.84	–12.20	0.100	10.22
	4.00	8.28	0.85	–6.15	0.648	4.26
	4.30	8.35	0.86	3.98	0.260	3.33
	5.00	8.28	0.88	19.30	0.889	94.97

With the addition of a polyelectrolyte solution in this series of experiments, the formation of flocs was intense and spectacular, and, as in the previous treatment, the use of slow stirring helped to achieve more efficient flocculation and then better settling. **Figure 2** illustrates the evolution of the optimal amount of chemicals as a function of zeta potential values.

An additional advantage of adding the treatment agent is that it does not shift the pH into the acidic range. Turbidity values decreased as they approached the optimal range. The specific electrical conductivity data did not increase significantly in proportion to the overdose of the treatment agent, similar to the turbidity value. That is, this treatment may be a good basis for treating larger volumes of greywater samples later. Based on all this, it is advisable to further study the conditions of treatment.

4.4. Scaling up, post-treatment, development of quality parameters

In a smaller volume, we determined the optimal amounts of chemicals only on 100 mL portions of the water to be treated with the help of a magnetic stirrer, while on a larger scale, a flocculator was used to assist. During scaling, we initially worked with 500 mL sample aliquots. The test sample aliquots were mixed at 300 rpm with the required multiple doses for both chemicals.

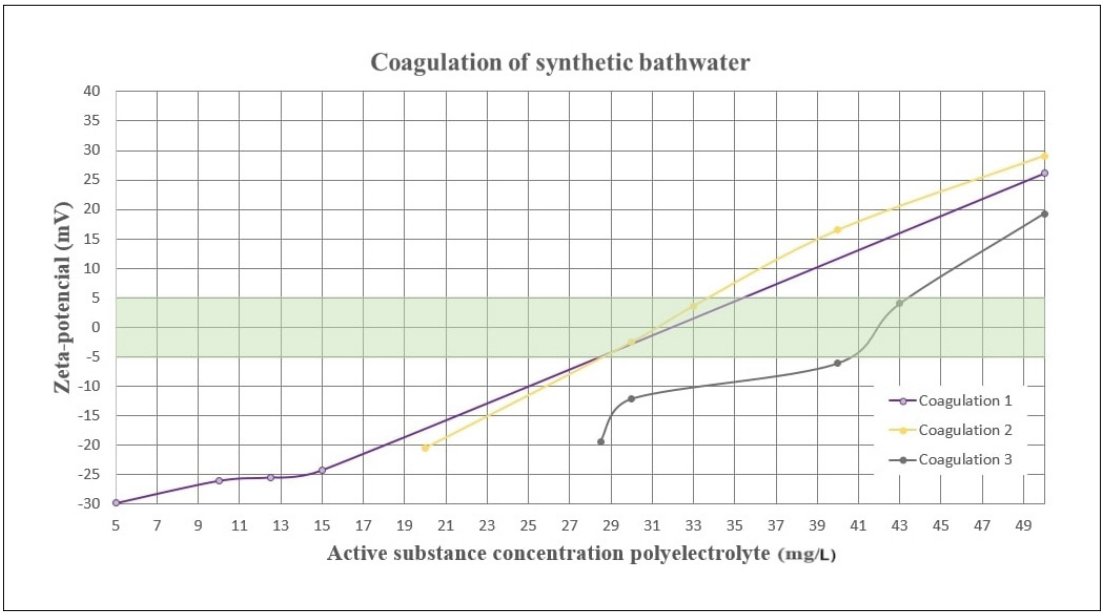

Figure 2. *Determination of the optimal amount of chemical in the case of polyelectrolyte stock solution.*

We found that the treatments performed well even in larger volumes, the previously determined optimum was sufficient for efficient contaminant removal, i.e. the examined greywater fraction can be treated well based on the scale increase. In our experiments, we also tested the coagulation-flocculation conditions and found that slow mixing for some time after chemical addition improves the formation of larger flocculants, so it is advisable to use it to produce better quality treated water.

Based on the experience with the 500 mL samples, we also performed our experiments on 1, 2, 3, and 4-litre samples. For larger volume samples, the sample was passed through a simple quartz sand filter after chemical treatment to remove settled contaminants. Based on all these, the **Tables 4–5.** summarizes the differences in the quality parameters of the untreated and coagulation-filtered water samples, thus characterizing the treatment efficiencies.

The tables well illustrate to us that although the two coagulants produced different data in two parameters, using the filtration as a post-treatment mechanism, almost the same quality of water is obtained as the result. The BOD5 and DOC values are the most prominent in the table, as it is clear how the chemical purification process takes place, i.e. how the content of contaminants in the water sample decreases.

Table 4. *Ferric chloride treatment agent and post-filtration water quality parameters*

$FeCl_3$	Raw sample	Treated sample	Filtered sample
pH	8.04	5.26	7.22
Specific electrical conductivity (mS/cm)	0.853	1.07	0.672
Zeta potential (mV)	–25.56	–4.76	–12.35
Turbidity NTU	10.02	3.93	0.20
BOI_5 (mg/L)	150	35	6
DOC (mg/L)	47.67	27.82	4.43

Table 5. *Polyelectrolyte treatment agent and post-filtration water quality parameters*

PE	Raw sample	Treated sample	Filtered sample
pH	7.92	8.15	7.83
Specific electrical conductivity (mS/cm)	0.946	0.925	0.754
Zeta potential (mV)	-30.50	4.38	-4.57
Turbidity NTU	54.05	6.33	0.17
BOI_5 (mg/l)	195	30	1.5
DOC (mg/l)	48.31	25.85	3.44

5. Summary

We have found that both treatment agents can be used effectively to treat greywater. Iron(III) chloride is an inexpensive and effective agent, but its use lowers the pH of the treated water, which may require subsequent neutralization. The polyelectrolyte type treatment agent is also effective even at lower doses, it does not lower the pH of the sample, but it is a more expensive material. Based on all this, it is advisable to further explore the treatment options and their possible new combinations to support sustainable water management.

References

[1] Kalmár F.: *Fenntartható energetika megújuló energiaforrások optimalizált integrálásával.* Akadémiai Kiadó, Budapest, 2014.

[2] Szabolcsik A., Bodnár I.: *A háztartásokban keletkező szürkevizek anion tartalmának meghatározása ionkromatográf segítségével.* Debreceni Műszaki Közlemények, Debrecen, 2014. [accessed on: 2021. 10. 18.] https://dea.lib.unideb.hu/dea/bitstream/handle/2437/212000/file_up_szabolcsik.pdf?sequence=1

[3] Dilip M. Ghaitidak &. Kunwar D. Yadav: „Characteristics and treatment of greywater—A review. Environmental Science and Pollution Research, 20/5. (2013) 2795–2809. https://doi.org/10.1007/s11356-013-1533-0

[4] Magyar Víziközmű Szövetség: Tájékoztató adat átlagfogyasztásról. 2019. https://www.maviz.org/tajekoztato_adat_atlagfogyasztasrol

[5] Bodnár Il.: *Vízgazdálkodás- és vízminőség védelem.* II. c. tantárgy oktatási segédlete. Környezetmérnöki Tanszék, DE-MK, Debrecen, 2018.

[6] Bodnár I.: *Oktatási segédlet a Környezetmérnöki méréstechnika és monitoring II. című tantárgy laboratóriumi gyakorlatához nappali és levelező tagozatos, környezetmérnök szakos hallgatók számára.* DE-MK, Környezet- és Vegyészmérnöki Tanszék, 2004–2015.

[7] ISO 2271:1989 szabvány: Felületaktív anyagok – Detergensek – Az anion aktív anyagok meghatározása kézi vagy mechanikus közvetlen kétfázisú titrálási eljárással, 1989.

[8] Bodnar I., Szabolcsik A., Baranyai E., Uveges A., Boros N.: *Qualitative Characterization of the Household Greywater in Northern Great Plain Region of Hungary.* Environmental Engineering and Management Journal, 13/11. (2014) 2717–2724.

sciendo

Acta Materialia Transylvanica 5/1. (2022) 29–34.
DOI: Hungarian: https://doi.org/10.33923/amt-2022-01-07
English: https://doi.org/10.33924/amt-2022-01-07

ACTA MATERIALIA TRANSYLVANICA

Investigation of the Effect of Over-Etching during Color Etching

József Bálint RENKÓ,[1] Péter János SZABÓ[2]

[1] *Budapest University of Technology and Economics, Department of Materials Science and Engineering, Faculty of Mechanical Engineering, Budapest, Hungary, renko.jozsef@edu.bme.hu*

[2] *Budapest University of Technology and Economics, Department of Materials Science and Engineering, Faculty of Mechanical Engineering, Budapest, Hungary, szpj@eik.bme.hu*

Abstract

During color etching, the examined grain structure undergoes a continuous, cyclic color change. This phenomenon is accompanied by a continuous loss of light intensity reflected from the surface. If the etching process is not stopped in time, the surface will be over etched. As a result, the separability of the individual grains will be greatly damaged, which can lead to a significant loss of information. It was investigated how to determine the moment of over-etching for each grain. During the in-situ observation of the etching, the time at which a particle can be considered over etched was determined by measuring the luminance normalized to the initial state.

Keywords: *color etching, metallography, Beraha I, microscopy, luminance, intensity, in-situ, steel.*

1. Introduction

Etching is a widely applied method for visualization of the microstructure of materials [1, 2]. since right after polishing, different phases and tissue elements cannot be separated. To make these species visible, different chemical and color etchants are needed [3, 4].

According to their mode of action, they can supply information for optical microscopic investigations in several ways. In most cases, the reactivity of the etchant is phase-sensitive, i.e., they can produce a chemical reaction only with certain phases [5]. With the help of this, the ratio of different phases present in the sample can be determined (Figure 1).

Within a given phase, the etchant can react with grains and grain boundaries with different velocities. Due to the disorder of the atoms along the grain boundaries, etchants can produce a faster reaction than inside the grains, therefore the grain structure of the material becomes visible. Grains themselves will also be etched during the process, but the speed of the etching is lower [6, 7].

The effect of color etchants is based on this latter phenomenon, since grains having different crystallographic orientations will be etched with different velocities. During the etching process, a precipitation film is formed on their surfaces, which produces thickness-dependent interference with the incoming light. Therefore, the grains of a polycrystalline material will be etched to different colors during a given time [8, 9].

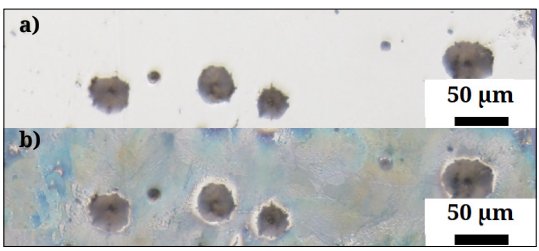

Figure 1. *Selective etching of spheroidal cast iron. Compared to the as-received state (a), Beraha I. etchant reacted only with the ferritic phase and not with the graphite (b).*

As the layer thickness increases, however, the rate of the color development decreases, until the surface will be over-etched. After this point the color change become almost negligible, and the grains can hardly be distinguished.

Since etching is an important part of metallic sample preparation, it is inevitable to adjust its parameters correctly if we want to obtain valuable information about the surface of the material. For this purpose, we performed in-situ observations during the etching process to determine the parameters of the overetching, and what are the connections between overetching and reflected light intensity.

2. Experimental

2.1. Materials and sample preparation

DC01 ferritic steel was investigated. The chemical composition of it was determined by a PMI-Master Sort type optical emission spectrometer. The results are shown in **Table 1**.

Cross section of the sample was then ground and polished. To minimize surface oxidation, etching was performed right after polishing **[10]**.

For etching the ferritic phase of DC01 steel, Beraha I etchant was used, which is a mixture of 3 g $K_2S_2O_5$, 10 g $Na_2S_2O_3$, and 100 ml distilled water **[11]**.

2.2. Microfluidic cell

For recording the color etching process, a closed channel system was created where the controlled laminar flow of the etchant can be ensured. The structure of the cell is shown in **Figure 2.a.** The cell itself was made of poly-dimethyl-siloxane (PDMS), to which a glass sheet was chemically bonded **[12]**. The channel system formed by these two parts is closed by the specimen itself, thus putting the cell below the objective lens of a microscope it becomes possible to follow the complete monitoring of the etching process (**Figure 2.b**).

Microscopic images were taken by an Olympus BX51 optical microscope. Dosing of the etchant during the process was performed by a syringe pump. The flow speed was set to 300 µl/min. Experiments were carried out in an air-conditioned laboratory, where the temperature was 21 °C.

3. Results and discussion

3.1. Color etching

To ensure the reach of the overetched state of the sample, the total etching time was set to 9 minutes. Starting from the arrival of the etchant into the cell, screen savings were made every 5th second from the video recorded during etching. Since the layer formation is relatively slow, this sampling frequency was enough to record the necessary characteristics. The etching process is shown in **Figure 3.**

Table 1. *Chemical composition of DC01 ferritic steel in weight%*

Fe	C	Mn	Cr	Mo
98.9	0.092	0.616	0.081	0.013
Ni	**Al**	**Co**	**Cu**	**Nb**
0.034	0.064	0.017	0.118	0.065

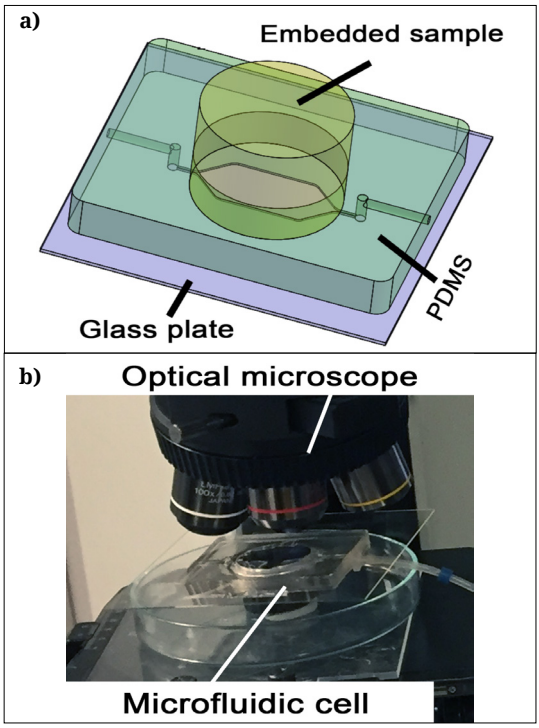

Figure 2. *Structure of the microfluidic cell (a) and the experimental assembly (b*

3.2. Determination of the moment of over-etching

25 grains were selected in the observed area, and the change of their colors was evaluated as the function of time (**Figure 4**).

The evaluation consisted of two parts. First, visual analysis was carried out on the selected grains to determine the exact time of their over-etching. A grain was determined to be overetched if no color change could be visually detected after 5, 10 or 15 seconds of etching. In the time interval of the experiment (540 sec) most of the selected grains were over-etched (exceptions were Nr. 3 and Nr. 5). Durations that were necessary for over-etching are shown in **Table 2.**

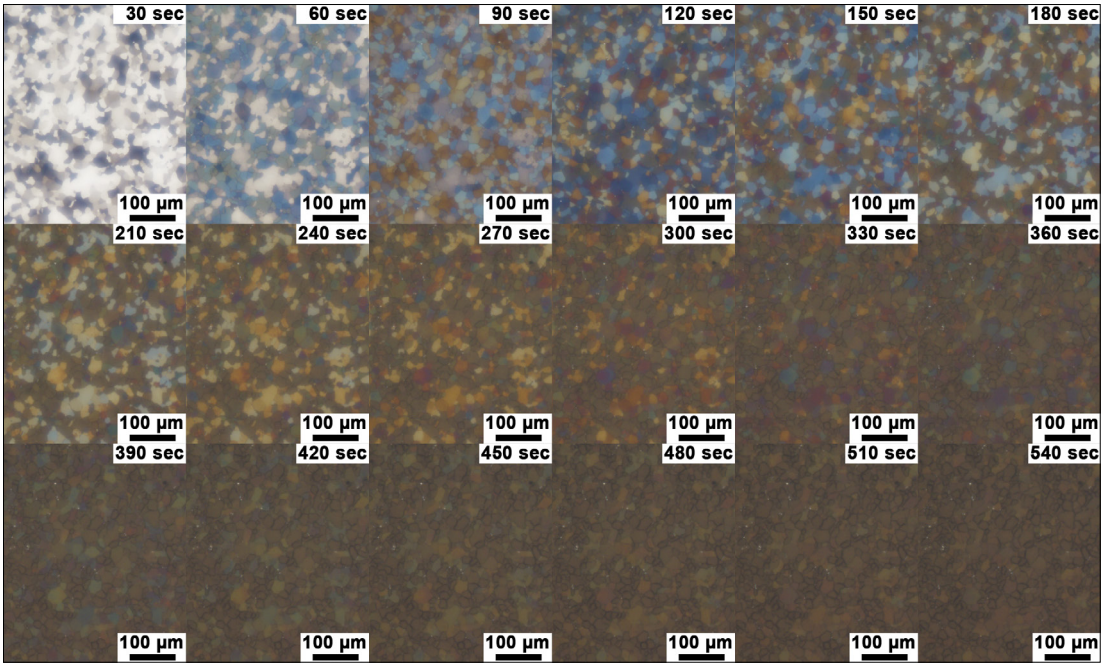

Figure 3. *Color etching of DC01 ferritic steel with Beraha I. etchant. Images were taken in every 30th seconds.*

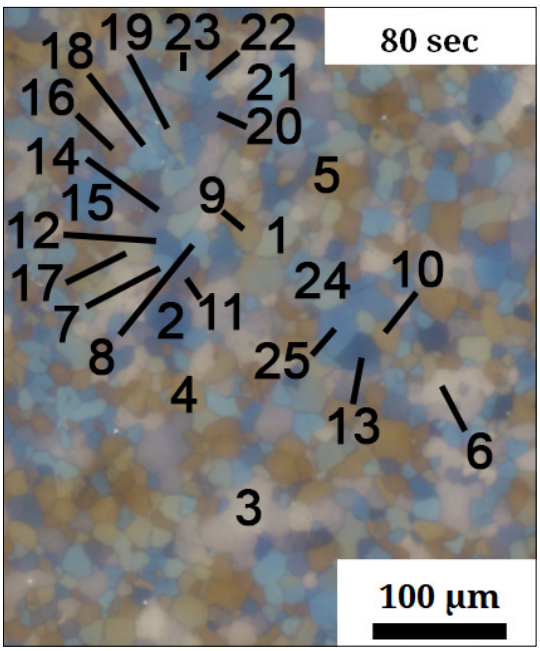

Figure 4. *The selected 25 grains of the examination.*

3.3. Intensity curves

In the second part of investigation, the RGB values of the individual grains were calculated by averaging the colors of the pixels within the grains [9]. Color intensity and luminescence are strongly affected by several factors, thus it was necessary to normalize the light intensities (having different wavelengths) to the initial state. The intensity values of the normalized intensity curves always started from 1 and fell into the range of [0,1].

RGB components (with different wavelengths) of different grains show a cosine-like monotonically decreasing amplitude. This phenomenon is illustrated for grain Nr. 1 in **Figure 5.**

In 2019, Bonyár divided the etching process into 3 parts, which can be observed in **Figure 5.** too [9]. The first is the oxide limited zone, the second is the steady state etching zone and the third is the diffusion limited zone. In the second one, which generally starts approx. from the first local minima, the etching speed of the grain becomes constant, thus the same time expires between the consecutive local minima and maxima of the normalized intensity curves. Before this one can observe the oxide limited part, where the initial oxide layer is being removed from the surface of the specimen. The oxide layer hinders the reaction between the etchant and the etched material, therefore reaching the first maxima requires more time.

Later during the etching process, the reaction speed will decrease again due to the increase of

Table 2. *The necessary time to reach the first minima and the over-etched state for the individual grains using visual observation, and the normalized luminance at these moments.*

#	Time (s)	Norm. lum. at first minima	Time (s)	Norm. lum. at over-etching
1	45	0.257	250	0.088
2	70	0.072	345	0.052
3	120	0,107	Out of range	
4	35	0.289	195	0.122
5	35	0.236	200	0.101
6	130	0.000	Out of range	
7	65	0.294	345	0.070
8	55	0.269	310	0.076
9	35	0.176	200	0.115
10	40	0.320	200	0.101
11	85	0.114	480	0.023
12	65	0.143	350	0.059
13	70	0.055	385	0.047
14	95	0.213	465	0.030
15	70	0.231	385	0.038
16	35	0.33	205	0.134
17	45	0.375	215	0.131
18	55	0.286	320	0.061
19	45	0.232	220	0.113
20	90	0.157	460	0.023
21	55	0.334	315	0.048
22	65	0.257	380	0.040
23	45	0.235	250	0.096
24	45	0.085	270	0.079
25	65	0.230	370	0.060

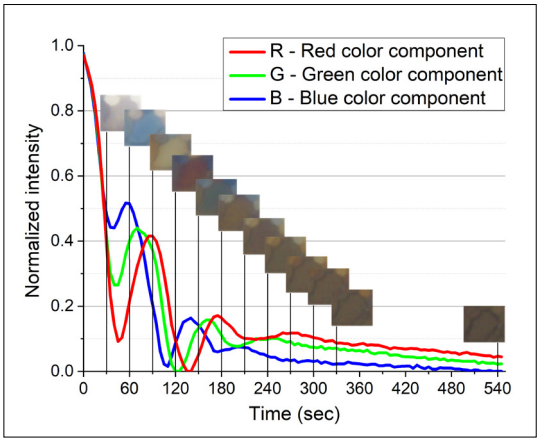

Figure 5. *Normalized color intensity of red (R), green (G) and blue (B) light reflected from grain Nr. 1 as a function of time.*

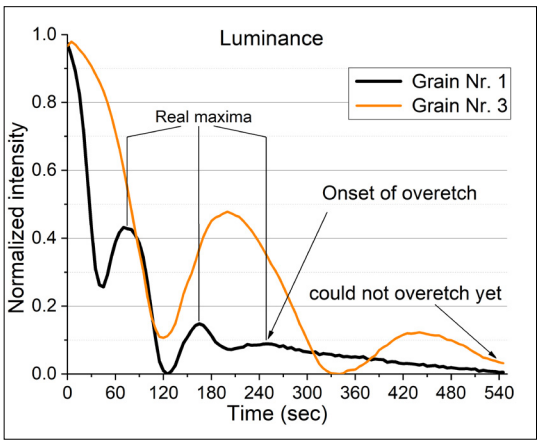

Figure 6. *Luminance curves of grains Nr. 1 and Nr. 3 as a function of time.*

the layer thickness. The formed layer, similarly to the oxide layer, also hinders direct contact between the etchant and the surface, thus the etchant must diffuse through the layer to react with the surface. As the layer thickness increases, the intensity of the reflected light also decreases, and the intensity differences between the individual grains slowly disappear. From that moment on, the sample is overetched.

In order to understand the process and obtain a more detailed picture, the onset of overetching must be determined using the measured intensity functions. To achieve this, the light intensity components must be investigated simultaneously. According to Eq. 1, a normalized brightness (luminance) was calculated from the individual RGB-components (**Table 2**).

$$L = 0{,}299 \cdot R + 0{,}587 \cdot G + 0{,}114 \cdot B \tag{1}$$

where L is the luminance, R,G and B are the intensity of the red, green, and blue light components **[13]**. Thus, light intensity curves for the investigated grains were determined (**Figure 6**). Initial maxima of the curves were neglected since the absolute maxima of the curves are irrelevant, only real (local) maxima were considered.

Luminance curves of the grains behave almost identically. Analyzing the curves of the chosen 25 points, they drop below 0.375 while reaching the first minima. This is followed by two and a half sine-like periods with decreasing amplitude. If the curve reaches the third real maxima, its slope becomes straight instead of cosine-like because the amplitude becomes too low.

3.4. Effect of over-etching

An interesting connection can be observed between the luminance curves and the onset of the over-etching: the later the over-etching happens, the smaller the light intensity that can be detected. The maximum value of luminance at the exact moment of over-etching for the examined grains was 0.134, but the average value of these was much smaller, only 0.075.

Besides this, in most cases (except grains Nr. 3 and Nr. 6, where the third maxima were not reached) the start of the overetching was detected right at the third real maxima. In other words, it started at the beginning of the previously introduced straight slope parts of the brightness curves.

The trends of normalized intensity curves of the same wavelength (i.e. red, green or blue) for different grains were similar, but the time necessary for reaching the local maxima was different according to the crystal orientation of the grains. This difference will result the separability of the grains. If we etch them for a certain amount of time, the layer thickness formed on the surfaces of the grains will be different, thus there will be different interference, i.e. different color on them. If, however, the specimen is being over-etched, the layer thickness will be uniform at the beginning of the over-etching, independently of the time needed for reaching the linear decreasing part of the intensity curve.

4. Conclusions

AIn the last period of color etching, the detectable light intensity decreases continuously due to over-etching, and thus the separability of the grains deteriorates. It was shown that over-etching starts at the third real maximum of the time-dependent normalized luminance curves. From this point, the slope of the curves lost its cosine characteristics and became linear. In the case of in-situ etching tests, this point should be avoided by stopping the process before reaching this.

Additionally, the more time needed to reach the onset of over-etching, the smaller will be the measured normalized luminance over the individual grains. Taking advantage of this effect, it could be possible to estimate the crystallographic orientation of these grains.

Acknowledgement

This work was supported by the ÚNKP-21-3-II-259 New National Excellence Program of the Ministry for Innovation and Technology from the source of the National Research, Development and Innovation Found. The research reported in this paper and carried out at BME has been supported by the NRDI Fund TKP2021 BME-NVA based on the charter of bolster issued by the NRDI Office under the auspices of the Ministry for Innovation and Technology.
Authors are grateful for the support of the NRDI Fund OTKA K 124926.

References

[1] Vander Voort G. F.: *Color Metallography*. Microscopy Today, 13/6. (2005) 22–27. https://doi.org/10.1017/S1551929500053943
[2] Mitra S.: *Sample Preparation for Microscopic and Spectroscopic Characterization of Solid Surfaces and Films.* In: Sample Preparation Techniques in Analytical Chemistry. (Ed: Somenath Mitra), Vol. 162. (2003) 377–411. https://doi.org/10.1002/0471457817.ch9
[3] Beraha E.: *Ätzmittel zur Sichtbarmachung chemischer und physikalischer Inhomogenitäten in Stahlgefügen*. Prakt. Metallogr., 4/8. (1967) 419–420.
[4] Petzow G.: *Metallographic Etching. Techniques for Metallography, Ceramography, Plastography,* ASM International, 1999, 1–240.
[5] Sato T., Takagaki T., Ikeda M., Nikaido T., Burrow M. F., Tagami J.: *Effects of Selective Phosphoric Acid Etching on Enamel Using "No-wait" Self-etching Adhesives.* J Adhes Dent. 20/5. (2018) 407–415. https://doi.org/10.3290/j.jad.a41359
[6] Szabó P. J., Kardos I.: *Correlation between grain orientation and the shade of color etching*. Materials Characterization, 61/8. (2010) 814–817. https://doi.org/10.1016/j.matchar.2010.05.005
[7] Vander Voort G.F.: *ASM Handbook. Metallography and Microstructures.* vol.9., 2004, 493–512.
[8] Kardos I., Gácsi Z., Szabó P. J.: *Color etching for characterization the grain orientation in spheroidal graphite cast iron.* Materials Science Forum, 389. (2007) 537–538.
[9] Bonyár A., Renkó J. B., Kovács D., Szabó P. J.: *Understanding the mechanism of Beraha-I type color etching: Determination of the orientation dependent etch rate, layer refractive index and a method for quantifying the angle between surface normal and the <100>, <111> directions for individual grains.* Materials Characterization, 156. (2019) 109844.
[10] Britz D.: *Opening the door to fundamental understanding of structure and color metallography - a correlative microscopy study on steel*. Microscopy and Microanalysis, (2014), 834.

[11] Beraha E.: Farbätzung für Gußeisen, Stähle, Werkzeugstähle, Manganstähle und ferritische und martensitische rostfreie Stähle, Prakt. Metallogr., 8/9. (1971) 547–550.
[12] Bonyár A., Sántha H., Ring B., Varga M., Kovács G. J., Harsányi G.: 3*D Rapid Prototyping Technology (RPT) as a powerful tool in microfluidic development*. Procedia Engineering, 5. (2010) 291–294. https://doi.org/10.1016/j.proeng.2010.09.105.
[13] Kaufmann M.: 5 - Contrast, brightness, CONTRAST, and BRIGHTNESS, The Morgan Kaufmann Series in Computer Graphics, Digital Video and HD (2nd Edition), (2012) 47–64. https://doi.org/10.1016/B978-0-12-391926-7.50005-9

Acta Materialia Transylvanica 5/1. (2022) 35–38.
DOI: Hungarian: https://doi.org/10.33923/amt-2022-01-08
English: https://doi.org/10.33924/amt-2022-01-08

High Heat Input Welding of NSSC 2120 Type Lean Duplex Steel

Soma Csaba SIMON,[1] Balázs VARBAI[2]

[1] *Budapest University of Technology and Economics, Faculty of Mechanical Engineering, Department of Materials Science and Engineering , Budapest, Hungary, simon.somacsaba@gmail.com*

[2] *Budapest University of Technology and Economics, Faculty of Mechanical Engineering, Department of Materials Science and Engineering , Budapest, Hungary,, varbai.balazs@gpk.bme.hu*

Abstract

Duplex stainless steels offer a high strength alternative to stainless steel, while providing excellent corrosion resistance, due to their dual-phase microstructure. This microstructure can be significantly influenced during welding, thus the maximum recommended heat input is usually 2.5 kJ/mm. In this research, we inspected the high heat input (3 kJ/mm) weldability of NSSC 2120 lean duplex stainless steel, which is designed and developed specifically for this purpose. The welds were evaluated by metallographic techniques and corrosion tests. It was found the NSSC 2120 grade can be welded with high heat input without deterioration in the phase balance and microstructure.

Keywords*: lean duplex stainless steel, electrochemical etching, microstructure.*

1. Introduction

Duplex stainless steels have high strength and excellent corrosion resistance due to their double (ferrite-austenitic) microstructure [1, 2]. However, the welding heat cycle can significantly influence the microstructure ratio, so the recommended heat input is usually no more than 2.5 kJ/mm [3]. During welding with a higher heat input, detrimental phase transformations and precipitations may appear in the ferrite phase [3].

The NSSC 2120 lean duplex was developed by the Japanese manufacturer for high heat input welding, primarily for submerged arc welding. According to the manufacturer's datasheet, no detrimental nitride precipitates appear in the heat-affected zone, which is particularly sensitive to phase transformation during high-heat welding [4]. In our research, welded seams were prepared with a heat input of 3 kJ/mm by the 135 welding process (GMAW) and were evaluated by metallographic methods and corrosion testing.

Table 1. *The chemical composition of NSSC 2120 lean duplex stainless steel, according to the manufacturer.*

C	Si	Mn	P	S
0.019	0.38	3.0	0.024	0.001
Ni	**Cr**	**Mo**	**Cu**	**N**
2.03	20.9	0.28	1.08	0.18

2. Materials and Methods

2.1. Base materials

For welding experiments, NSSC 2120 lean duplex plates (not standardized) with a thickness of 10 mm were used. The chemical composition of the base material according to the manufacturer's data sheet is shown in Table 1 .

2.2. Welding consumables

Two types of welding wires were used for the welding experiments, both Ø 1.2 mm size. The solid wire recommended for welding standard duplex steels was G 22 9 3 N L (22 % Cr, 9 % Ni, 3 % Mo) and the flux cored wire recommended for welding lean duplex steels was T 23 7 N L R M/C 3 (23 % Cr, 7 % Ni, rutile flux). The welding wires are hereinafter referred to as 2209 and 2304 (Avesta FCW-2D 2304), respectively, according to the manufacturer's designation.

2.3. Welding parameters

Welding experiments were performed using the 135 welding process (GMAW) using a Yaskawa welding robot and a Fronius TPS 400i Pulse power supply. The seams were welded by pulsed material transfer with the PMC Universal process version of the power source, which provides a uniform penetration depth. The heat input for wire 2209 was 3.05 kJ/mm with a thermal efficiency of 0.8, and for wire 2304 it was 2.99 kJ/mm. A gas mixture of M12 - ArC - 2.5 (argon + 2.5% CO_2) with a flow rate of 15 l/min was used as shielding gas in both cases.

2.4. Microstructural evaluation methods

The ferrite content of the welds was measured with a Fischer Feritscope FMP30 type ferrite scope. The weld geometry dimensions were measured on a metallographic sample with an Olympus SZX16 stereo microscope. The metallographic samples were prepared first by grinding to a grain size of 4000 and then by polishing with a 3 µm diamond suspension. Microstructural images were taken with an Olympus PMG3 optical microscope. Electrochemical etching was performed on samples prepared for metallographic examination. For oxalic acid etching, 10 g of reagent ($C_2O_4H_2$) was dissolved in 90 ml of distilled water, and etching was performed at 7 V for 15 seconds. For nitric acid electrochemical etching, 60 ml of nitric acid (HNO3) was mixed with 40 ml of distilled water, and etching was performed at 2 V for 20 seconds.

2.5. Corrosion testing methods

Corrosion tests were performed according to the ASTM 1084 standard [5] for lean duplex steels. The 25 × 50 mm samples were placed in a solution containing 55.1 g of ferrous chloride ($FeCl_3 \cdot 6H_2O$), 6.6 g of sodium nitrate ($NaNO_3$) and 600 ml of distilled water for 24 hours. the corrosion rate and the pitting corrosion behaviour were determined from the weight loss. The weight of the samples was measured on a Denver Instrument APX-200 with an accuracy of 0.1 mg.

3. Results and discussion

3.1. Results of the weld geometry measurements

The face width of the 2209 solid wire weld was 14.5 ± 0.6 mm and the face height was 4.1 ± 0.2 mm. The penetration depth measured on the cross-section was 5.4 mm and the weld cross section area was 84.1 mm^2. The form factor calculated by dividing the penetration depth by the face width was thus 0.37.

The seam welded with 2304 flux cored wire had a face width of 15.9 ± 0.6 mm and a face height of 3.3 ± 0.3 mm. The penetration depth measured on the cross-section was 3.2 mm and the weld cross section area was 60.1 mm^2. The form factor calculated by dividing the penetration depth by the face width was thus 0.19.

The results show that although the heat input was roughly the same (~ 3 kJ/mm in both cases), a much smaller weld volume was deposited in the case of the flux cored wire, which is due to the presence of many slag-forming materials in the flux with the same wire diameter, which is not included in the volume of the weld metal.

3.2. Results of the microstructural evaluations

The ferrite content measured with a ferrite scope was 40.5±5.5 % for the weld metal welded with 2209 solid wire. For the 2304 flux cored wire, this value was 41.5±6.8 %. The values correspond to the ferrite content specified in MSZ EN ISO 17781 [6] (minimum 30 % and maximum 70 %), therefore NSSC 2120 can be welded well in terms of phase ratio with high heat input and the use of both wires.

Oxalic acid electrochemical etching can be used to detect carbides and nitrides in ferrite according to ASTM A1084 standard [5] Carbide and nitride precipitates appear as a dark area after etching, for the proportions of which the standard contains comparative images. The images after oxalic acid etching are shown in Figure 1 for solid wire 2209 and in Figure 2 for flux cored wire 2304.

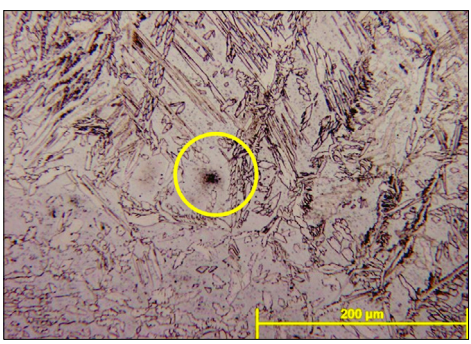

Figure 1. *Weld metal welded with 2209 wire and heat affected zone after oxalic acid electrochemical etching. A sign indicating nitride precipitation in the heat zone is shown in a black circle.*

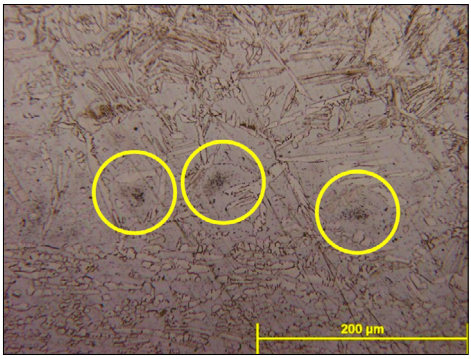

Figure 2. *Weld metal welded with 2304 wire and heat affected zone after oxalic acid electrochemical etching. A sign indicating nitride precipitation in the heat zone is shown in a black circle.*

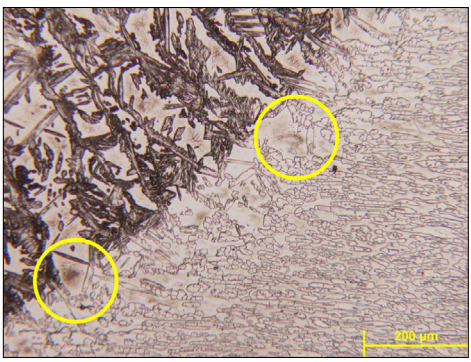

Figure 3. *Weld metal welded with 2209 wire and heat affected zone after nitric acid electrochemical etching. A sign indicating nitride precipitation in the heat zone is shown in a yellow circle.*

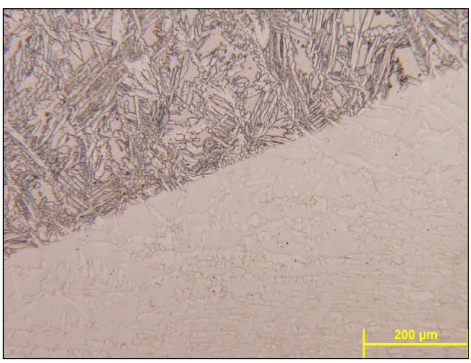

Figure 4. *Weld metal welded with 2304 wire and heat affected zone after nitric acid electrochemical etching. No signs of nitride precipitations.*

Minimal signs of carbide or nitride precipitation were found during etching (circled in the figures) and are abundant in the appropriate category according to the referenced standard. The electrochemical etching with nitric acid for the detection of various intermetallic phases and nitride precipitations was performed according to the ASTM E407 standard **[7].** The images following nitric acid etching are shown in **Figure 3.** for solid wire 2209 and **Figure 4** for flux cored wire 2304. Minimal signs of nitride precipitation were found during etching (circled in the figures), which are also compliant according to the referenced standard.

Based on the microstructure evaluation, it can be stated that the NSSC 2120 grade can be welded well with a heat input of 3 kJ/mm according to the manufacturer's recommendations, and the heat zone is less sensitive to the formation of detrimental secondary phases.

3.3. Results of the corrosion testing

The results of the corrosion test are shown in **Table 2.** The corrosion rate was 0.64 g/m^2 for solid wire 2209 and 0.72 g/m2 for flux cored wire 2304, which corresponds to the maximum 4 g/m^2 for welds, according to the MSZ EN ISO 17781 standard.

Table 2. *Results of the corrosion testing*

	2209 wire	2304 wire
Weight before test	61,0167 g	59,8156 g
Weight after 24 hours	61,0159 g	59,8147 g
Weight loss	0,0008 g	0,0009 g

4. Conclusions

In our research, we investigated the weldability of NSSC 2120 lean duplex steel with high heat input. Gas metal arc welding experiments were performed with a heat input of 3 kJ/mm, using solid wires of 2209 and a flux cored wire of 2304. Based on the evaluation of the welds, it can be stated that the ferrite content is suitable in the weld metal in both cases, nitride precipitation in the heat affected zone is not typical, and the corrosion resistance of the welds are accepted according to the immersion tests.

Acknowledgements

We are grateful to Flexman Robotics Kft. For using the Yaskawa robot required for welding. This paper has been supported by the National Research, Development and Innovation Office – NKFIH, OTKA PD 138729.

References

[1] Uzonyi S., Asztalos L., Dobránszky J.: *Duplex korrózióálló acél durvalemezek hegesztése.* Műszaki Tudományos Közlemények 3. (2015) 315–318. https://doi.org/10.33895/mtk-2015.03.71

[2] Kovács D., Blücher J., Fábián E. R., Dobránszky J.: *Nemesíthető acélok és rozsdamentes acélok plazmanitridálása.* Műszaki Tudományos Közlemények, 5. (2016) 237–240. https://doi.org/10.33895/mtk-2016.05. 50

[3] Kotecki D. J.: *Some Pitfalls in Welding of Duplex Stainless Steels.* Soldagem & Inspeção, 15. (2010) 336–343. https://doi.org/10.1590/S0104-92242010000400011

[4] New Lean Duplex NSSC®2120. https://stainless.nipponsteel.com/en/campaigns/duplex/orientation/nssc2120.php (accessed on: 2022. 04. 22.)

[5] ASTM A1084-15a: Standard Test Method for Detecting Detrimental Phases in Lean Duplex Austenitic/Ferritic Stainless Steels, 2015.

[6] MSZ EN ISO 17781:2018: Kőolaj-, petrolkémiai és földgázipar. Vizsgálati módszerek a ferrites/ausztenites (kettős) korrózióálló acélok minőség-ellenőrzésére, 2018.

[7] ASTM E407-07(2015)e1: Standard Practice for Microetching Metals and Alloys, 2015.

sciendo

Acta Materialia Transylvanica 5/1. (2022) 39–44.
DOI: Hungarian: https://doi.org/10.33923/amt-2022-01-09
English: https://doi.org/10.33924/amt-2022-01-09

ACTA MATERIALIA TRANSYLVANICA

Development of a Novel Hybrid Manufacturing Technology for Continuous Fiber-Reinforced Thermo-Plastic Composites

Csenge TÓTH,[1] Norbert Krisztián KOVÁCS[1,2]

[1] *Budapest University of Technology and Economics, Faculty of Mechanical Engineering, Department of Polymer Engineering, Budapest, Hungary*

[2] *MTA–BME Lendület Lightweight Polymer Composites Research Group, Budapest, Hungary, kovacsn@pt.bme.hu*

Abstract

In this study, we present a novel approach for the production of continuous fiber-reinforced thermoplastic composites by combining injection molding and additive manufacturing. After exploring the design requirements, we manufactured inserts via continuous fiber-reinforced 3D printing, then we used them as reinforcement for injection-molded samples. Improper fiber placement can cause warpage as the continuous fibers prevent shrinking; however, warpage can be compensated with the insert geometry. The reinforcement resulted in an increase of about 30 % in the properties tested.

Keywords: *additive manufacturing, injection molding, fiber-reinforced polymer composite.*

1. Introduction

The additive manufacturing of continuous fiber-reinforced composites is one of the fastest growing polymer manufacturing technologies today. 3D-printed composites have the advantage of designable fiber orientation (even along several degrees of freedom [1], but the technology has not yet reached its potential in terms of mechanical properties, and cycle times are still relatively high [2, 3].

On the other hand, injection molding is one of the fastest ways of producing thermoplastic composites. The common practice in the industry is still the use of short fibers, and to increase the length several methods have been reported lately [4, 5]. However, besides the fiber length, the orientation is also important to achieve the desired increase in mechanical properties. The orientation is determined by the melt flow direction, which does not necessarily coincide with the stress directions [6, 7]. The need therefore arises for tailorable fiber properties in injection-molded composites.

Technologies for continuous fiber-reinforced injection-molded products have also emerged [8, 9]. Usually, the fiber-reinforced preform or sheet is placed in the mold and then the thermoplastic polymer matrix is injected onto it [10]) Usually, the fiber-reinforced preform or sheet is placed in the mold and then the thermoplastic polymer matrix is injected onto it. The procedure is often referred to as overmolding as well [11, 12]. The sheets are mostly reinforced thermoplastic laminates with a specific fabric orientation and layup sequence, which provides the strength and stiffness comparable to that of thermosetting composites, however, this type of reinforcement is restricted in terms of design freedom. Fiber placement and orientation in the product is strictly determined and the fiber content can only be varied by the number of laminas.

Extrusion-based additive manufacturing of continuous fiber-reinforced composites might be a promising alternative. 3D printing can be used to create customized reinforcing structures directly where stresses apply, thus reducing material and the costs as well [13].

In this research, we investigate the applicability of 3D-printed composites for overmolding. We present the design requirements of a 3D-printed composite insert and the property modifying effects of the continuous fibers in the injection-molded product.

2. Materials and methods

2.1. Materials

For the 3D-printed inserts, Markforged "Tough Nylon" (later called "End of life Nylon") filament was used as matrix material. The filament is stored in a drybox. Markforged Continuous Carbon Fiber filament was used as reinforcement [14], According to the literature, the filament contains 1000 single fibers [15].

For injection molding (overmolding) Alphalon 27 type PA6 was used from Grupa Azoty ATT Polymers [16]. Before molding the granulate was dried at 80 °C for 4 hours based on the manufacturer's recommendations.

2.2. Methods

The inserts were prepared with a Mark Two (Markforged, USA) type FFF-based composite 3D printer. For slicing, the company's cloud-based software (Eiger) was used. Main printing parameters are shown in Table 1 where the values fixed in the slicer are marked. Parameters regarding the matrix material (Fill pattern and Fill density) were set to produce a solid structure with as few voids as possible. The fiber reinforcement was placed along the outer walls. We aimed to achieve the maximum fiber content at minimum wall thickness applicable, thus creating strong and lightweight inserts. The different insert geometries allowed for different amounts of fiber to be placed, therefore fiber volume fractions also varied. The fiber volume fractions were determined with Eq. (1) and the volumes were calculated within the slicer.

$$v_f = \frac{V_f}{V_c} \tag{1}$$

where V_f (cm^3) is the fiber volume content and V_c (cm^3) is the composite volume.

Before injection molding, simulations were run for the "U" and "K" type inserts using Moldflow (Autodesk, 2016). The aim of the simulations was to visualize the melt flow around the inserts and to determine the mold temperature that could theoretically ensure the conditions for polymer bonding. CAD models were prepared dusing Autodesk Inventor Professional (Autodesk, 2020) and the meshes were prepared in Hypermesh (Altair Hyperworks, 2017.1).

Injection-molded specimens were prepared with an Arburg Allrounder Advance 270S 400-170 injection molding machine at zone temperatures of 255 °C, 260 °C, 265 °C, 270 °C, 270 °C, a mold temperature of 80 °C and an injection pressure of 1500 bar. The injection molding parameters were determined based on the simulation results and the manufacturer's recommendations [16].

Table 1. *Printing parameters*

Parameter	value
Fill pattern	Solid
Fill density	100 %
*Fill orientation	45°
Fiber infill type	concentric
*Nozzle diameter	0.4 mm
*Nozzle temperature	270 °C

Quasi-static flexural tests were performed on a Zwick Z005 type machine according to the MSZ EN ISO 178 standard [17] on at least 5 samples. Support distance was 64 mm and the test speed was 5 mm/s.

3. Design of the composite inserts

3.1. Geometry

Continuous fiber-reinforced inserts were designed for injection-molded specimens with the purpose of increasing the flexural properties. Three main groups of requirements were defined for the insert geometries. First, the design must meet the printability requirements determined by the equipment and the slicing software. Second, the geometry must be applicable for overmolding which imposes constraints on geometry (simply put, it should fit the mold) and material use (the inserts must withstand the shear, pressure, and temperature of the polymer melt). Finally, the end product must have adequate bonding between the matrix and the reinforcement that lasts until failure, and the inserts must enhance one or more chosen mechanical properties.

First, two types of inserts were designed as shown in Figures 1a–b. Then, based on the experiences of the first overmolding, a third geometry was also designed (Figure 1c). For each type, the fibers are placed parallel with the longitudinal axis, so that the reinforcement is in the part of the product most exposed to stress. The placement of an insert in the mold can be seen in Figure 2. The tolerance of the external dimensions is designed for a tight fit so that the inserts do not fall out during mold closing. Fiber volume fractions of the inserts are shown in Table 2.

Table 2. *Fiber volume fractions of the inserts*

Insert type	vf (%)
U	26,9
K	8,3
W	10,5

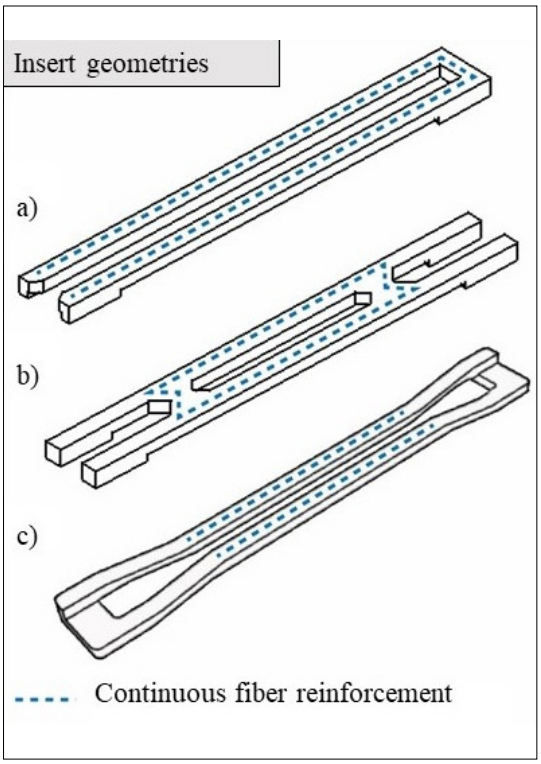

Figure 1. *Schematics of the insert geometries: a) type "U" b) type "K" c) type "W". The dashed line indicates the planned placement of the continuous fiber reinforcement*

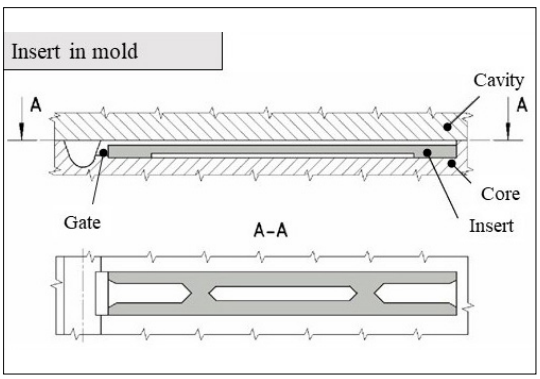

Figure 2. *Schematics of the type "K" insert in the mold.*

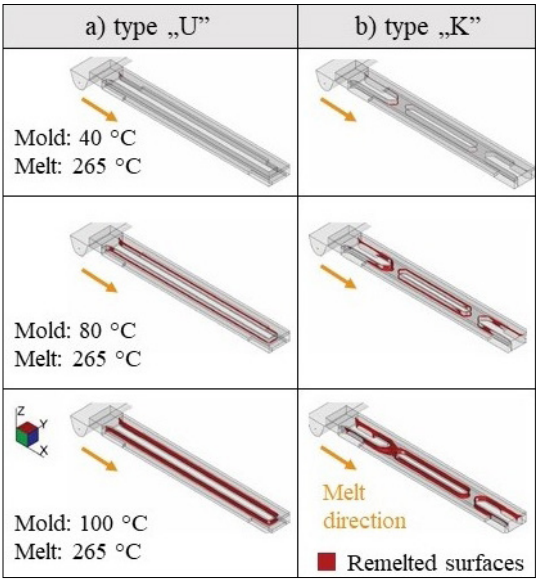

Figure 3. *Remelted surface areas as a function of mold and melt temperature.*

3.2. Injection molding simulations

Injection molding simulations were run to gain information about the melt flow and the expected bonding between the inserts and the injection-molded matrix.

The remelted surface areas of the inserts were examined as a function of mold temperature. Results can be seen in **Figure 3.** As expected, the amount of remelted surface areas will increase with higher temperature, therefore – assuming the use of compatible materials – better bonding can be expected. These results can provide the basis for the selection of the injection molding parameters. It can also be seen that the injected melt is expected to fill the gaps around and within the inserts. This is of great importance as voids would serve as failure locations.

4. Insert preparation and injection molding

The inserts were 3D printed, then placed in the mold manually. Then the matrix material was injected around the inserts. The first overmolding experiments showed a significant warping of the specimens. This is because after ejection the polymer shrinks, but the continuous carbon fibers do not, therefore the fiber reinforcement blocks the deformation where it is placed. Thus, in case of asymmetric fiber placement, the degree of shrinkage differs at the sides of the sample which

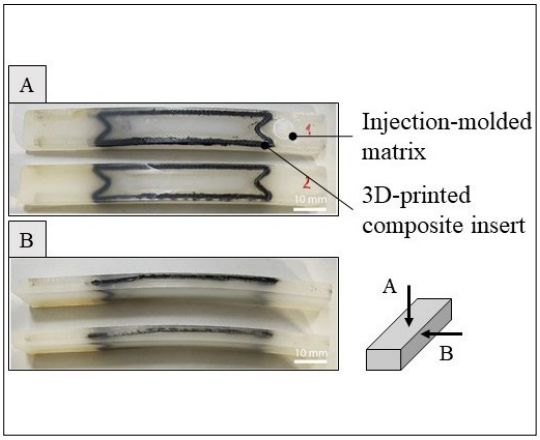

Figure 4. *Injection-molded specimen reinforced with type "K" insert*

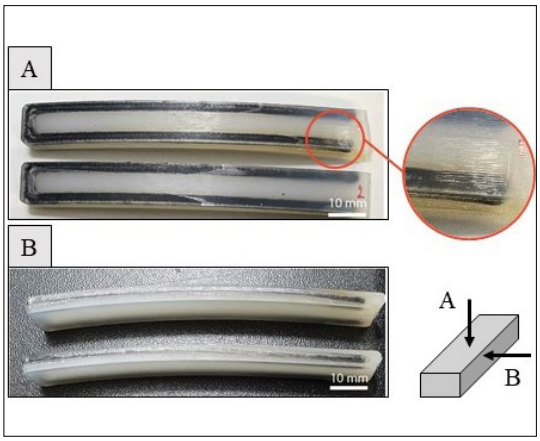

Figure 5. *Injection-molded specimen reinforced with type "U" insert*

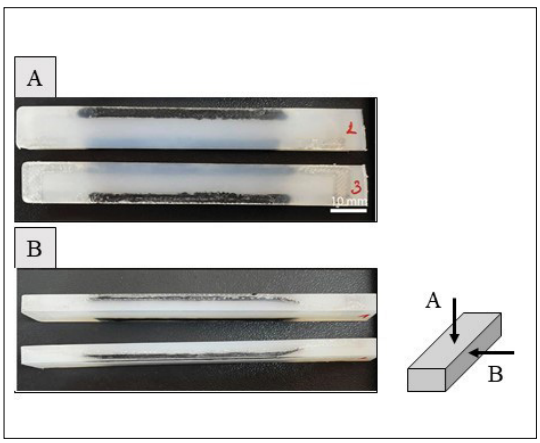

Figure 6. *Injection-molded specimen reinforced with type "W" insert*

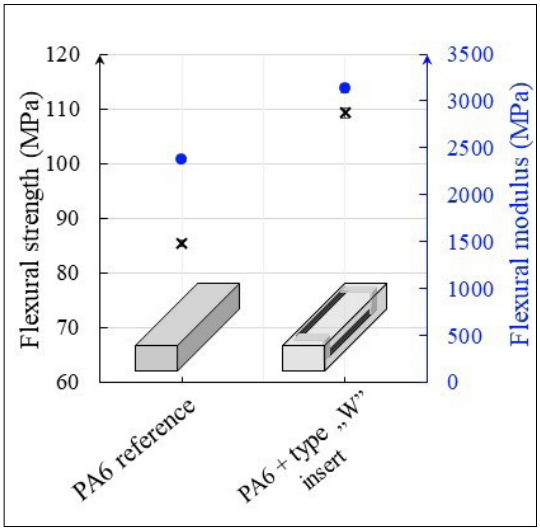

Figure 7. *Flexural strength and modulus of the unreinforced reference and the composite samples*

results in warpage. Figure 4 and 5 shows the injection-molded specimens reinforced with the type "K" and "U" inserts, respectively. Warpage is clearly visible in both cases.

A slight change in color can be seen along the walls of the inserts, similar to the burn marks of the diesel effect (Figure 5). There can be several reasons for this. The inserts may have prevented proper ventilation, and the entrapped gas caused ignition and therefore thermal degradation. The shear forces near the gate could also exceed the limit of the 3D-printed polymer. These results show that overmolding requires different parameters than traditional injection molding, and one must consider the material parameters of the inserts as well.

To compensate warping, a third insert geometry (type "W") was designed, in which equal amounts of reinforcing fibers are placed along the opposite sides. The symmetric fiber placement compensated shrinking and therefore warpage was visibly reduced (Figure 6).

5. Flexural mechanical properties

3-point bending was performed to investigate the effect of the reinforcement on the flexural mechanical properties. Results can be seen in Figure 7 Due to the warping of the type „U" and type „K" reinforced samples, only the type „W" specimens could be tested. It can be seen that the inserts increased the flexural stress and the mod-

ulus by approximately 30 %. The relatively small standard deviations suggest that the technology is well reproducible.

6. Conclusions

In this study, a novel hybrid technology is presented for the production of continuous fiber-reinforced thermoplastic composites. Carbon fiber-reinforced structures were produced with 3D printing, then the composites were placed in the mold and the polymer matrix was injected on them. Injection molding simulations were also run before sample preparation. It was found that improper fiber placement can cause warpage as the continuous fibers prevent shrinking, however, it was also presented that warpage can be compensated with the insert geometry. The composites produced with overmolding showed a 30 % increase in flexural strength and modulus compared to the unreinforced samples. Overall, the hybrid technology presented offers the potential for the productive manufacture of recyclable, continuous fibre-reinforced products with the possibility of customization as well.

Acknowledgements

This work was supported by the Hungarian Scientific Research Fund (OTKA FK134336).

References

[1] van de Werken N., Tekinalp H., Khanbolouki P., Ozcan S.: *Additively manufactured carbon fiber-reinforced composites: State of the art and perspective*. Additive Manufacturing, 31 (2020) 100962. https://doi.org/10.1016/j.addma.2019.100962

[2] Liu S., Li Y., Li N.: *A novel free-hanging 3D printing method for continuous carbon fiber reinforced thermoplastic lattice truss core structures*. Materials and Design, 137. (2018) 235–244. https://doi.org/10.1016/j.matdes.2017.10.007

[3] Wang X., Jiang M., Zhou Z., Gou J., Hui D.: *3D printing of polymer matrix composites: A review and prospective*. Composites Part B: Engineering, 110. (2017) 442–458. https://doi.org/10.1016/j.compositesb.2016.11.034

[4] Tábi T., Égerházi A. Z., Tamás-Bényei P., Czigány T., Kovács J. G.: I*nvestigation of injection moulded poly(lactic acid) reinforced with long basalt fibres.* Composites Part A: Applied Science and Manufacturing, 64. (2014) 99–106. https://doi.org/10.1016/j.compositesa.2014.05.001

[5] Yan X., Cao S.: *Structure and interfacial shear strength of polypropylene-glass fiber/carbon fiber hybrid composites fabricated by direct fiber feeding injection molding*. Composite Structures, 185. (2018) 362–372. https://doi.org/10.1016/j.compstruct.2017.11.037

[6] Yu S., Hwang J. Y., Hong H. S.: *3D microstructural characterization and mechanical properties determination of short basalt fiber-reinforced polyamide 6,6 composites*. Composites Part B: Engineering, 187. (2020) 107839. https://doi.org/10.1016/j.compositesb.2020.107839

[7] Sun X., Lasecki J., Zeng D., Gan Y., Su X., Tao J.: *Measurement and quantitative analysis of fiber orientation distribution in long fiber reinforced part by injection molding*. Polymer Testing, 42. (2015) 168–174. https://doi.org/10.1016/j.compositesb.2020.107839

[8] Valvedere M. A., Kupfer R., Wollmann T., Kawashita L. F., Gude M., Hallett S. R.: *Influence of component design on features and properties in thermoplastic overmoulded composites.* Composites Part A: Applied Science and Manufacturing, 132. (2020) 105823. https://doi.org/10.1016/j.compositesa.2020.105823

[9] Schneider T.: *Lightweight construction: First composite gearbox housing with layer-optimized organo sheeting weighs 30 % less than a comparable aluminum component*. Reinforced Plastics, 63/1. (2019) 40–45. https://doi.org/10.1016/j.repl.2017.11.018

[10] Karakaya N., Papila M., Özgoc G: *Overmolded hybrid composites of polyamide-6 on continuous carbon and glass fiber/epoxy composites: An assessment of the interface.* Composites Part A: Applied Science and Manufacturing, 131. (2020) 105771. https://doi.org/10.1016/j.compositesa.2020.105771

[11] Fu L., Zhang M., Zhai Z., Jiang F.: The influence of preheating temperature on the mechanical properties of injection-overmolded hybrid glass fiber reinforced thermoplastic composites. Polymer Testing, 105. (2022) 107425. https://doi.org/10.1016/j.polymertesting.2021.107425

[12] Andrzejewski J., Przyszczypkowski P., Szostak M.: *Development and characterization of poly(ethylene terephthalate) based injection molded self-reinforced composites. Direct reinforcement by overmolding the composite inserts.* Materials&Design, 153. (2018) 273–286. https://doi.org/10.1016/j.matdes.2018.04.084

[13] Boros R., Rajamani P. K., Kovács J. G.: *Combination of 3D printing and injection molding: Overmolding and overprinting*. eXPRESS Polymer Letters, 13/10. (2019) 889–897. https://doi.org/10.3144/expresspolymlett.2019.77

[14] www.markforged.com (elérés: 2022. 03. 10.).

[15] Dickson A. N., Barry J. N., McDonnell K. A., Dowling D. P.: *Fabrication of continuous carbon, glass and Kevlar fibre reinforced polymer composites using additive manufacturing*. Additive Manufacturing, 16. (2017) 146–152. https://doi.org/10.1016/j.addma.2017.06.004

[16] https://grupaazoty.com/en/group-s-offer/plastics/alphalon-27 (elérés: 2022. 03. 10.).
[17] MSZ EN ISO 178: Műanyagok. A hajlítási tulajdonságok meghatározása, 2010.

sciendo

Acta Materialia Transylvanica 5/1. (2022) 45–51.
DOI: Hungarian: https://doi.org/10.33923/amt-2022-01-10
English: https://doi.org/10.33924/amt-2022-01-10

ACTA MATERIALIA TRANSYLVANICA

Analysis of Thermogravimetric and Dynamic Mechanical Properties of PLA/PBS Blends Doped with Zinc Oxide Nanoparticles

Ábris Dávid VIRÁG,[1] Kolos MOLNÁR[2,3]

[1] *Budapest University of Technology and Economics, Faculty of Mechanical Engineering, Department of Polymer Engineering. Budapest, Hungary, viraga@pt.bme.hu*

[2] *Budapest University of Technology and Economics, Faculty of Mechanical Engineering, Department of Polymer Engineering. Budapest, Hungary*

[3] *MTA–BME Research Group for Composite Science and Technology. Budapest, Hungary, molnar@pt.bme.hu*

Abstract

In the present work, PLA-PBS blends of 80/20 weight ratio were doped with zinc oxide (2.5; 5; 7.5 and 10 phr) and the flow, thermogravimetric and thermomechanical behaviour of the resulting blends were investigated. Using capillary plasstometry, thermogravimetry (TGA) and dynamic mechanical analysis (DMA), it was found that the increase in zinc oxide content resulted in an increase in the flow indices (MFI, MVR), as well as in the storage and loss modulus values, and a decrease in the thermal stability and glass transition temperature.

Keywords*: PLA, blends, zinc-Oxide, thermogravimetry.*

1. Introduction

Polylactic acid (PLA) is one of the most widely used biodegradable polymers today. Its popularity is demonstrated by the fact that, according to the Web of Science database [1] 7301 new research articles containing the term PLA or polylactic acid in their title were published in 2021 and 6867 in 2020.

Much of this research is related to the use of PLA as a packaging material, as about 40 % of the polymers produced are used as packaging materials, which are generally single-use and have a very short life cycle due to their function [2]. In general, polylactic acid (PLA) has properties comparable to those of currently used bulk polymers, but it is a very brittle base material with poor gas barrier properties and is therefore poorly suited for food packaging applications (without plasticisers or other additives) [3]. The brittleness can be addressed by blending PLA with various tough materials, preferably also biodegradable polymers (e.g. polybutylene succinate (PBS), polybutylene adipate terephthalate (PBAT)). Furthermore, to improve the gas barrier properties, it is advisable to use various nanoadditives, such as zinc-oxide (ZnO). Zinc-oxide is a multifunctional, environmentally friendly nanoadditive, which is classified by the US Food and Drug Administration as a „Generally Recognised as Safe" (GRAS) additive, i.e. it can be used in food packaging [4]. In addition, a number of studies have confirmed that zinc-oxide improves the gas barrier properties of the material [5], and has antibacterial [6], and even to some extent antiviral [7, 8] properties.

In the present study, we investigated the extent to which the thermogravimetric and thermomechanical properties of tista PLA are modified by blending with PBS and by the addition of zinc-oxide to the blend.

2. Materials and methods

2.1. Preparation of test samples

The specimens required for the tests were prepared using Ingeo Biopolymer 2500HP polylactic acid (PLA) manufactured by Natureworks LLC, PBE 003 polybutylene succinate (PBS) manufactured by NaturePlast, and Zincweiss Reszsiegel ME-004 zinc-oxide (ZnO).

The compounds were prepared using a Labtech Engineering Co., Ltd. (Thailand) LTE 26-44 twin screw extruder. The temperatures of the 10 zones

of the extruder were as follows: 190/190/190/190/190/190/200/200/210/210.

The screw rotation speed was 25 rpm and the feed speed was 5 rpm. The zinc-oxide (2.5; 5; 7.5 and 10 phr), measured to the nearest two tenths of a gram, was mechanically mixed with a dry mixture containing 80 % PLA and 20 % PBS, respectively. This mixture was then fed into the extruder in order to obtain a more uniform distribution of the ZnO nanoparticles.

After exiting the extruder, the extrudate was passed through a fibre conveyor while being cooled by cooling fans mounted above the conveyor, and finally granulated using a Labtech Engineering (Thailand) LZ-120/VS. Thus, the test samples shown in **Table 1** were prepared. It is important to note that in the table phr (parts per hundred rubber) means the amount of zinc-oxide added to 100 mass units of polymer.

Table 1. *Prepared test samples and their ZnO content*

Sample name	PLA %	PBS %	ZnO	
			phr	%
PLA	100	100	0	0
PBS	0	0	0	0
PLA/PBS/0	80	20	0	0
PLA/PBS /2,5	78.0	19.5	2.5	2.4
PLA/PBS/5	76.2	19.0	5	4.8
PLA/PBS/7,5	74.4	18.6	7.5	7
PLA/PBS/10	72.7	18.2	10	9.1

For energy dispersive spectroscopy and dynamic mechanical tests we needed pressed plates, which were prepared on a Teach-Line Platen Press 200E hydraulic press from Dr. Collin GmbH (Germany). For pressing we use a press frame of 160x160x1 mm. The pressing temperature was 210 °C. The pressing process consisted of the following steps: preheating at 0 MPa for 3 minutes, followed by pressing at 0.98, 1.96 and 2.94 MPa for 1-1 minute (opening the die for glass evaporation and closing between steps), and finally pressing at 3.92 MPa for 3 minutes and cooling.

2.2. Test methods

The Melt Flow Index (MFI) and Melt Volume Rate (MVR) were measured using Instron CEAST 7027.000 machine, with 5 measurements per type of material. The measurements were performed at 210 °C (final temperature of the compounding) with a load of 2.16 kg in accordance with MSZ EN ISO 1133 **[9]**.

Energy-dispersive spectroscopy (EDS) was performed on cryogenic array surfaces coated with a thin gold layer using a JEOL JSM 6380LA scanning electron microscope (SEM) manufactured by Jeol Ltd.

The thermal stability and the evolution of thermal decomposition processes were analysed by thermogravimetric analysis (TGA) (according to MSZ EN ISO 11358-1 **[10]** The tests were carried out on 5-10 mg samples, using a TA Instruments Q500 machine in the temperature range 50 to 600 °C at a heating rate of 10 °C/min.

Dynamic mechanical tests were carried out using a TA Instruments Q800 machine with temperature sweeps ranging from subambient to 150 °C at a heating rate of 2 °C/min. For each measurement, an amplitude was chosen that was within the linear viscoelastic range. The tests were performed using a dual cantilever beam arrangement, with 10x60 mm samples cut from precut sheets. Temperature sweeps were carried out on both the neat polymers and the compounds, however, the blends containing 7.5 and 10 phr zinc-oxide were so brittle that they broke during capture.

3. Results

3.1. Energy dispersive spectroscopy

EDS was also used to investigate the zinc-oxide content and distribution in the blends, EDS images of the pure PLA/PBS blend and blends containing 2.5;5;7.5 and 10 phr zinc-oxide are shown in **Figures 1–5.** The red dots in the figures indicate the zinc particles. The PLA/PBS blend does not contain zinc-oxide, the red dots in the figure only indicate measurement noise. In the case of the 2.5

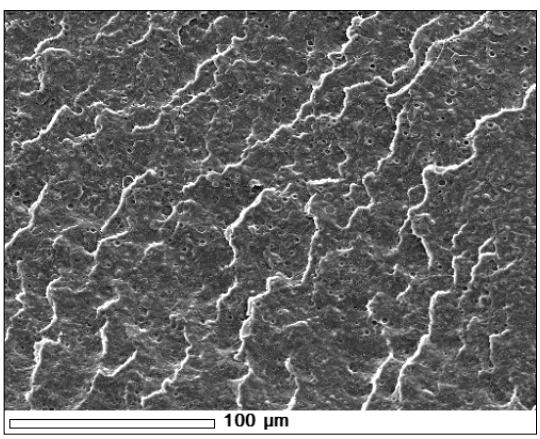

Figure 1. *SEM micrograph of PLA/PBS mixture.*

phr blend, zinc-oxide particles are already visible and evenly distributed in the blend. For the 5 and 7.5 phr blends, the amount of zinc-oxide increases, but the distribution of zinc-oxide is not as uniform, with zinc-oxide aggregates being observed in the polymer matrix. Finally, in the case of the 10 phr blend, zinc-oxide is present in larger aggregates. As the zinc-oxide content increases, the uniform distribution of particles deteriorates spectacularly. The resulting aggregates cause the polymer matrix to be discontinuous, creating potential defect sites.

As can be seen from **Figures 1–5** the careful preparation of the base material resulted in a particularly good dispersion at 2.5 and 5 phr ZnO content, but even so, the 5 phr aggregated ZnO particles with a high surface/volume ratio still failed to disperse properly.

Table 2 shows the content of zinc (Zn) and zinc-oxide (ZnO) for the different Kev products. Only the amount of Zn can be determined directly in the measurement, the equimolar amount of oxygen must be added to the amount of zinc to determine the ZnO content. The atomic mass of zinc is 65.38 g, the oxygen is 16 g. In this case, for every 65.38 g of zinc there is 16 g of oxygens, so that 65.38 g of zinc actually corresponds to 81.38 g of zinc-oxide. That is, 1 mass ratio zinc corresponds to 1.24 mass ratio zinc-oxide. Having made this correction, it can be seen from **Table 2** that the values obtained are almost identical to the amount added. For the 2.5; and 5 phr zinc-oxide,

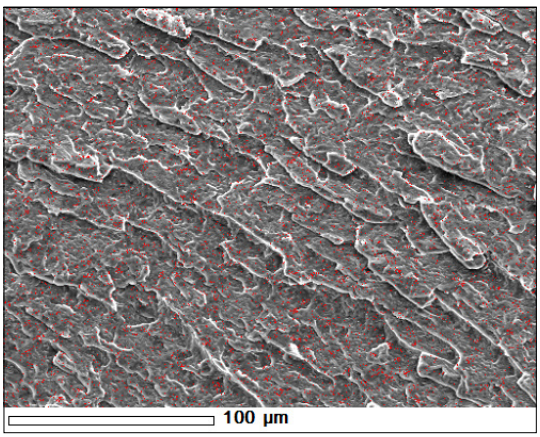

Figure 2. *SEM micrograph of a PLA/PBS blend containing 2.5 phr ZnO (red colour indicates Zn element).*

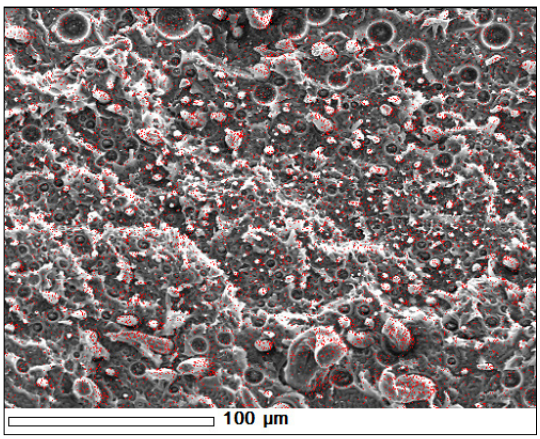

Figure 4. *SEM image of a PLA/PBS mixture containing 7.5 phr ZnO (red colour indicates Zn element).*

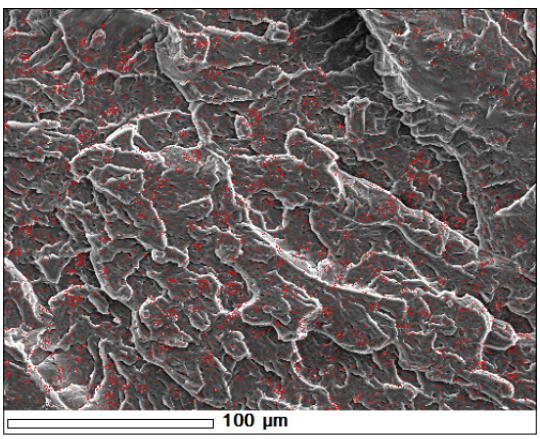

Figure 3. *SEM image of a PLA/PBS mixture containing 5 phr ZnO (red colour indicates Zn element).*

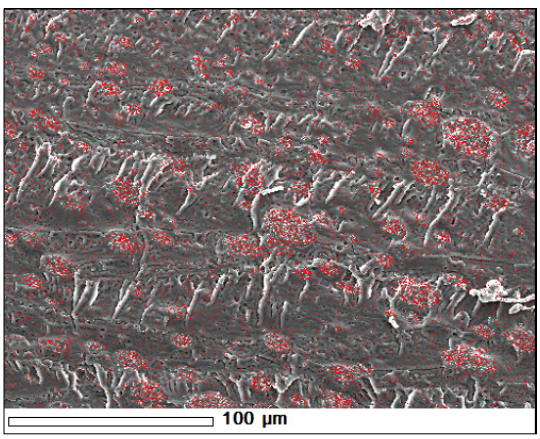

Figure 5. *SEM image of a PLA/PBS mixture containing 10 phr ZnO (red colour indicates Zn element).*

Table 2. *Zn and ZnO content of blend and compounds.*

Sample name	Zn	ZnO	Added ZnO
PLA/PBS/0	0.02±014	0.02±0.02	0
PLA/PBS/2.5	1.82±0.10	2.26±0.12	2.44
PLA/PBS/5	3.87±0.13	4.80±0.16	4.76
PLA/PBS/7.5	5.16±0.10	6.40±0.12	6.98
PLA/PBS/10	5.64±0.13	7.00±0.16	9.09

Table 3. *Melt Flow Index and Melt Volume Rate for the tested materials/*

Sample name	MFI (g/600 s)	MVR (cm^3/600 s)
PLA	8.06±0.13	7.31±0.10
PBS	3.42±0.95	3.26±0.91
PLA/PBS	8.55±0.12	7.81±0.16
PLA/PBS/2,5	58.85±4.33	73.91±14.13
PLA/PBS/5	60.38±2.85	70.74±13.82

the calculated results are almost identical to the amount added. However, at higher ZnO contents, the distribution of particles is not uniform, aggregates remain in the blend, which explains the discrepancy between the added and measured data. It can be seen that the higher the zinc-oxide content, the greater the discrepancy.

3.2. Thermogravimetric analysis

The results of the MFI measurements are presented in **Table 3** The average of the measured PLA values is the same as the 8 g/600 s reported in the data sheet **[11]** PBS produced lower values compared to those in the datasheet **[12],** but the MFI determination of 5 g/600 s in that datasheet was made at 190 °C. A small increase in the average MFI value of the PLA/PBS blend was observed, however, a jump-like increase in both MFI and MVR was observed with the addition of zinc-oxide. This jump-like increase indicates a significant degradation. The increase in the flow properties with increasing zinc-oxide content was so significant that the waiting and residence times for the 5 phr mixture had to be reduced. Although the 2.5 phr ZnO mixture was still measurable, such an increase in MFI could cause problems during processing. Measurement of the 7.5 and 10 phr mixtures was not possible even with parameter changes.

3.3. Thermogravimetric analysis

The thermal stability of the samples was investigated using TGA, the results of the test are shown in **Figures 6** and **7** and **Table 4** mutatja. The decomposition process was carried out in one step for PLA, PBS and blend, and in two steps for zinc-oxide doped compounds. The heights of the steps indicate the PLA and PBS content, respectively. The thermal decomposition of pure PBS started at a higher temperature (344 °C) than the decomposition of PLA (309 °C). These results indicate that PBS is more resistant to thermal degradation than PLA. The thermal stability of the PLA/PBS blend was higher than that of pure PLA, which means that PBS has an effect on thermal stability, as confirmed by Jompang et al **[13]**.

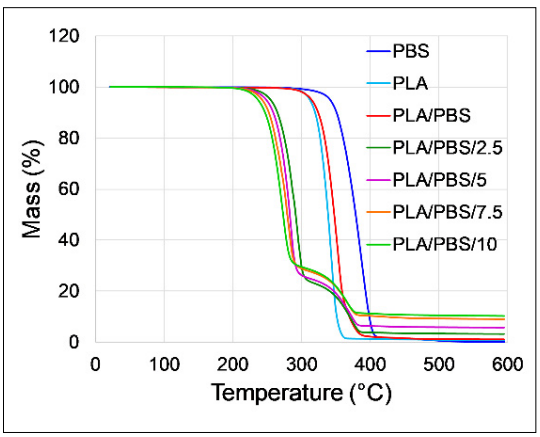

Figure 6. *Thermogravimetric curves of the tested materials.*

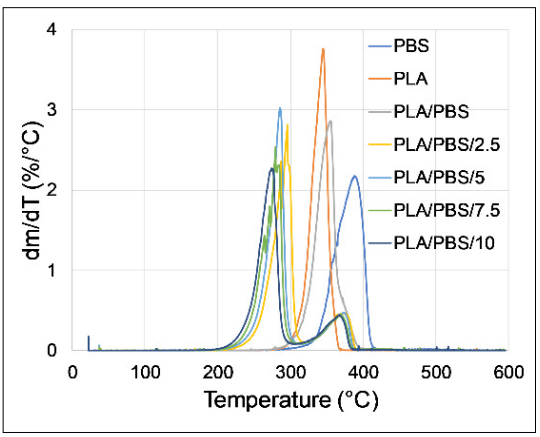

Figure 7. *Differential thermogravimetric curves of the tested materials.*

Table 4. *Quantified results of thermogravimetric analysis*

	PBS	PLA	PLA/PBS	PLA/ PBS/2,5	PLA/PBS/5	PLA/ PBS/7,5	PLA/ PBS/10
Number of stages	1	1	1	2	2	2	2
Start point of the 1st stage, A1 (°C)	344	309	310	256	251	241	236
End point of the 1st stage, B1 (°C)	402	352	365	301	291	288	286
End point of the 2nd stage, A2 (°C)	–	–	–	347	345	344	339
End point of the 2nd stage, B2 (°C)	–	–	–	384	381	378	376
1st loss in mass (%)	100	99.2	98.9	77.5	75.5	72.6	71.5
2nd loss in mass (%)	–	–	–	19.3	18.8	18.4	18.2
Residue (%)	0.03	0.82	1.06	3.19	5.71	9.00	10.28
Corrected residue (%)	–	–	0	2.13	4.65	7.94	9.22
1st peak on the DTG curve (°C)	387	343	352	294	284	280	273
2nd peak on the DTG curve (°C)	–	–	–	374	373	369	367

The thermal decomposition of ZnO-containing compounds started at increasingly lower temperatures with increasing zinc-oxide content. The large decrease in thermal stability indicates that ZnO has a strong degradation effect on PLA at high temperatures.

The corrected residual (corrected here means corrected by the mass remaining in the PLA/PBS blend) values show the ZnO content of the sample. It can be seen that these values are in good approximate agreement with the EDS determined and the coated ores (**Table 2**).

At the same time, it can be observed that the increasing zinc-oxide content only slightly reduced the thermal stability of the PBS phase.

3.4. Dynamic mechanical analysis

The results of the DMA tests are shown in **Figures 8–10.** A strange anomaly is observed in the PBS curve around 30 °C, however, it can be seen that around 105 °C there is a drastic decrease in the storage and loss modulus values, indicating the crystallization temperature of PBS. For the blend and the compounds, it can be seen that around 60 °C the storage modulus drops drastically (since this is where the glass transition temperature of PLA is located), and then around 80 °C the storage modulus starts to increase again. This increase can be explained by the cold crystallization of PLA. It can also be seen that around 110 °C there is a decrease in the curves, possibly due to the fact that at this temperature the PBS particles melt and enter the melt state, but after this the storage modulus values continue to increase until the cold crystallisation takes place. From the curves, it can also be seen that the storage and loss modulus values increase with the limit of blending compared to pure PLA, and further increase with increasing the amount of zinc-oxide content. The values of the glass transition temperatures (T_g) determined by MSZ EN ISO 6721 **[14]** based on the maximum loss factor are given in

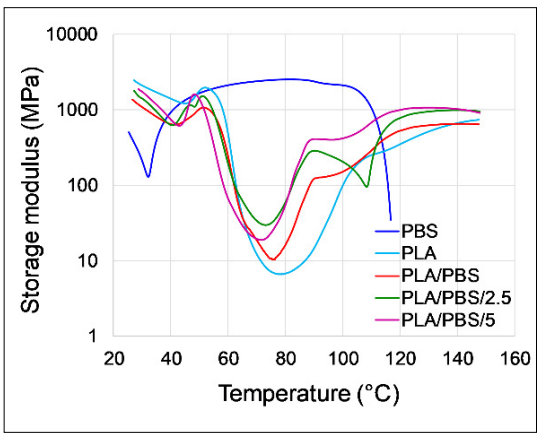

Figure 8. *Storage modulus curves of the tested materials.*

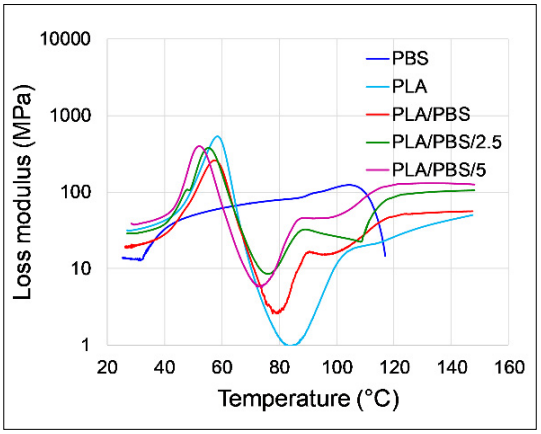

Figure 9. *Loss modulus curves of the tested materials.*

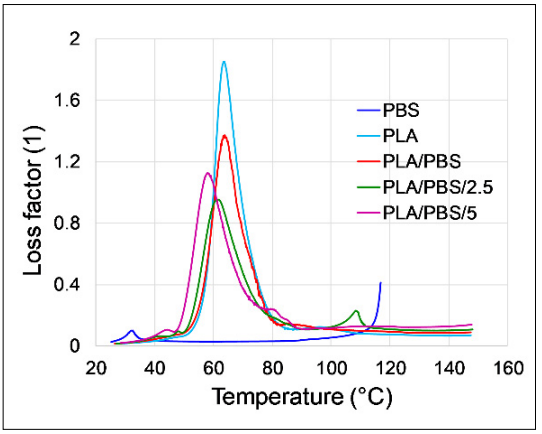

Figure 10. *Loss factor curves of the tested materials.*

Table 5. The table shows that the glass transition temperature of the blend did not change compared to pure PLA, but that the glass transition temperature of the blend decreased slightly with increasing zinc-oxide content.

Table 5. *Glass transition temperature of PLA and blends*

Sample name	T_g (°C)
PLA	63.4
PLA/PBS	63.9
PLA/PBS/2,5	61.2
PLA/PBS/5	58.1

4. Conclusions

In the present work, PLA-PBS blends (in 80-20 mass ratio) were doped with zinc-oxide (2.5; 5; 7.5 and 10 phr) and the flow, thermogravimetric and thermomechanical behaviour of the resulting blends were investigated. Using energy dispersive spectroscopy, it was found that there was no significant difference between the amount of zinc-oxide added and the actual ZnO present in the material up to 5 phr, but that this difference increased with increasing zinc-oxide content above 5 phr due to the ZnO aggregates. The MFI and MVR values of the tested blend increased drastically with increasing zinc-oxide content. It can be concluded that zinc-oxide caused a significant degradation of the material. This was also confirmed by the TGA results, which showed a decrease in the thermal stability of the blend with increasing zinc-oxide content, by 54 °C for 2.5 phr and by 74 °C for 10 phr. The dynamic mechanical tests showed that the storage and loss modulus values increased with blending compared to pure PLA, and further increased with increasing the zinc-oxide content. Overall, it can therefore be concluded that with increasing the amount of zinc-oxide added to the 80-20 % PLA/PBS blend, the flowability increases dramatically, the thermal decomposition temperature decreases significantly, the storage and loss modulus values increase and the glass transition temperature decreases slightly.

Acknowledgements

The research was supported by the ÚNKP-21-3 and ÚNKP-21-5 New National Excellence Programme of the Ministry for Innovation and Technology, from the source of the National Research, Development and Innovation Fund and the Bolyai János Research Grant of the Hungarian Academy of Sciences. The research was funded by the National Research, Development and Innovation Office (NKFIH OTKA FK138501).

References

[1] https://www.webofscience.com/wos/woscc/advanced-search (accessed on: 2022. 02. 28.)
[2] PlasticsEurope, Plastics: the Facts 2021, https://plasticseurope.org/knowledge-hub/plastics-the-facts-2021/ (letöltve: 2022. 02. 28.)
[3] Sonchaeng U., Iniguez-Franco F., Auras R., Selke S., Rubino M., Lim L.: *Poly(lactic acid) mass transfer properties.* Progress in Polymer Science, 86/11. (2018) 85–121. https://doi.org/10.1016/j.progpolymsci.2018.06.008
[4] Matai I., Sachdev A., Dubey P., Uday Kumar S., Bhushan B., Gopinath P.: Antibacterial activity and mechanism of Ag–ZnO nanocomposite on S. aureus and GFP-expressing antibiotic resistant E. coli. Colloids and Surfaces B: Biointerfaces, 115/3. (2014) 359–367.

https://doi.org/10.1016/j.colsurfb.2013.12.005
[5] Reddy K. M., Feris K., Bell J., Wingett D. G., Hanley C., Punnoose A.: Selective toxicity of zinc oxide nanoparticles to prokaryotic and eukaryotic systems. Applied Physics Letters, 90/5. (2007) 213902–213903.
https://doi.org/10.1063/1.2742324
[6] Sharma R., Jafari S. M., Sharma S.: *Antimicrobial bio-nanocomposites and their potential applications in food packaging*. Food Control, 112/6. (2020) 1–11.
https://doi.org/10.1016/j.foodcont.2020.107086
[7] Merkl P., Long S., McInerney G. M., Sotiriou G. A.: *Antiviral Activity of Silver, Copper Oxide and Zinc Oxide Nanoparticle Coatings against SARS-CoV-2*. Nanomaterials, 11/5. (2021) 1–9.
https://doi.org/10.3390/nano11051312
[8] Mizielinska M., Nawrotek P., Stachurska X., Ordon M.: *Packaging Covered with Antiviral and Antibacterial Coatings Based on ZnO Nanoparticles Supplemented with Geraniol and Carvacrol*. International Journal of Molecular Sciences, 22/4. (2021) 1–14.
https://doi.org/10.3390/ijms22041717
[9] ISO 1133: Plastics — Determination of the melt mass-flow rate (MFR) and melt volume-flow rate (MVR) of thermoplastics, 2011.
[10] ISO 11358: Plastics — Thermogravimetry (TG) of polymers, 2014.
[11] Ingeo™ Biopolymer 2500HP Technical Data Sheet, https://www.natureworksllc.com/~/media/Files/NatureWorks/Technical-Documents/Technical-Data-Sheets/TechnicalDataSheet_2500HP_extrusion_pdf.pdf?la=en (accessed on: 2022. 03. 01.)
[12] Natureplast PBE-003 Technical Data Sheet, (letöltve: 2022. 03. 01.)
http://natureplast.eu/wp-content/uploads/2019/03/190319-Material-Portfolio-ENG.pdf
[13] Jompang L., Thumsorn S., On J. W., Surin P., Apawet C., Chaichalermwong T., Kaabbuathong N., O-Charoen N., Srisawat N.: *Poly(lactic acid) and poly(butylene succinate) blends fibers prepared by melt spinning technique*. Energy Procedia, 34/3. (2013) 493–499.
https://doi.org/10.1016/j.egypro.2013.06.777
[14] ISO 6721: Plastics — Determination of dynamic mechanical properties, 2019.